



This is the accepted manuscript made available via CHORUS. The article has been published as:

## Coexistence of single-particle and collective excitation in $^{61}\text{Ni}$

xmlns="http://www.w3.org/1998/Math/MathML">mmultiscripts>mi>Ni/mi>mprescripts>/mprescripts>none>/none>mn>61/mn>/mmultiscripts>/math>

Soumik Bhattacharya, Vandana Tripathi, E. Rubino, Samuel Ajayi, L. T. Baby, C. Benetti, R.

S. Lubna, S. L. Tabor, J. Döring, Y. Utsuno, N. Shimizu, J. M. Almond, and G. Mukherjee

Phys. Rev. C **107**, 054311 — Published 22 May 2023

DOI: [10.1103/PhysRevC.107.054311](https://doi.org/10.1103/PhysRevC.107.054311)

# Coexistence of single particle and collective excitation in $^{61}\text{Ni}$

Soumik Bhattacharya , Vandana Tripathi , E. Rubino, Samuel Ajayi, L. T. Baby, C. Benetti, R. S. Lubna, S. L. Tabor  
*Department of Physics, Florida State University, Tallahassee, Florida, 32306, USA\**

J. Döring  
*Bundesamt für Strahlenschutz, D-10318 Berlin, Germany*

Y. Utsuno  
*Advanced Science Research Center, Japan Atomic Energy Agency, Tokai, Ibaraki 319-1195, Japan and  
Center for Nuclear Study, University of Tokyo, Hongo, Bunkyo-ku, Tokyo 113-0033, Japan*

N. Shimizu  
*Center for Computational Sciences, University of Tsukuba, 1-1-1 Tennodai, Tsukuba 305-8577, Japan*

J. M. Almond  
*Physics Division, Oak Ridge National Laboratory, Oak Ridge, TN 37831, USA*

G. Mukherjee  
*Variable Energy Cyclotron Centre, Department of Atomic Energy, 1/AF Salt Lake City, Kolkata-700064, India  
(Dated: May 5, 2023)*

The high spin states in  $^{61}\text{Ni}$  have been studied using the fusion evaporation reaction,  $^{50}\text{Ti}(^{14}\text{C},3n)^{61}\text{Ni}$  at an incident beam energy of 40 MeV. A Compton suppressed multi-HPGe detector setup, consisting of six Clover detectors and three single crystal HPGe detectors was used to detect the de-exciting  $\gamma$  rays from the excited states. The level scheme has been extended up to an excitation energy of 12.8 MeV and a tentative  $J^\pi = 35/2^+$ . The low-lying negative parity levels are found to be generated by single particle excitation within the  $fp$  shell and also excitations to the  $g_{9/2}$  orbitals as explained well with shell model calculations using the  $\text{GXPF1Br}+V_{MU}$  (modified) interaction. Two rotational structure of regular E2 sequences with small to moderate axial deformation have been established at higher excitation energy. Most interestingly, two sequences of M1 transitions are reported for the first time and described as magnetic rotational bands. The shears mechanism for both the bands can be described satisfactorily by the geometrical model. The shell model calculation involving the cross shell excitation beyond the  $fp$  shell well reproduce the M1 and E2 sequences. The shell model predicted  $B(M1)$  values for the magnetic rotational band B1 show the decreasing trend with spin as expected with closing of the shears.

## I. INTRODUCTION

Neutron-rich nuclei with  $A \approx 60$  have attracted the attention of experimental and theoretical studies in the last few decades because of the evolution of shell structure with the  $N/Z$  value in this region. On one hand, from the systematic studies of  $2_1^+$  energies and  $B(\text{E2}:2_1^+ \rightarrow 0_1^+)$  strengths, a new sub-shell closure has been established at  $N = 32$  in  $^{52}\text{Ca}$  [1],  $^{54}\text{Ti}$  [2], and  $^{56}\text{Cr}$  [3]. Contrary to that, the decreasing trend of the  $2_1^+$  and  $4_1^+$  energies towards  $N = 40$  [4, 5], for both the Fe and Cr isotopic chains point to the diminishing of the  $N = 40$  sub-shell closure for mid-shell nuclei between the  $Z=20$  and 28 major shell-closures. For  $Ni$  isotopes, the  $Z = 28$  major shell closure stabilizes the spherical shapes near the ground state between  $N = 28$  and  $N = 40$ , and the low and moderate energy states can be well reproduced by shell-model calculations involving the  $\nu p_{3/2}$ ,  $\nu f_{5/2}$ ,  $\nu p_{1/2}$

and  $\nu g_{9/2}$  orbitals [6, 7]. Though the  $N=40$  subshell closure is visible in  $^{68}\text{Ni}$  [8], the energy gap between the  $1p_{1/2}$  and  $0g_{9/2}$  orbitals is estimated to be small to allow the cross-shell excitations in  $^{68,67}\text{Ni}$  which are well reproduced by shell-model calculations [6, 9]. The involvement of the shape driving  $\nu 0g_{9/2}$  orbital induces collectivity in lighter  $Ni$  isotopes, and rotational bands have been observed in  $^{56-59}\text{Ni}$  [10–13]. Furthermore, magnetic rotational bands and super-deformed bands have also been reported in  $^{60}\text{Ni}$  [14] and  $^{63}\text{Ni}$  [15], respectively. Recently, excited states in  $^{61}\text{Ni}$  have been studied experimentally [16] via a  $^7\text{Li}$  induced reaction and the energy levels could be explained fairly well within the scope of shell-model calculation involving cross-shell excitations to  $0g_{9/2}$  single-particle orbital.

The odd-mass  $Ni$  isotopes with neutron number slightly over  $N = 28$  are ideal cases to address the role of neutron  $g_{9/2}$  excitations at high spin. In the investigation of  $^{59}\text{Ni}$  [13] four rotational bands up to a probable spin of  $(43/2)$  with terminating properties were found. Based on configuration-dependent cranked Nilsson-Strutinsky calculations, two bands maintained significant collectiv-

---

\* corresponding author : soumik.kgpiit@gmail.com

ity until the maximum spin was reached. In  $^{63}\text{Ni}$  three collective bands up to spin and parity of  $(57/2^+)$  were identified [15]. Model calculations of cranked Nilsson-Strutinsky type indicate that in  $^{63}\text{Ni}$  collective excitations sustain at moderate and high spins. The shears mechanism in  $^{60}\text{Ni}$  has been described microscopically with the self-consistent tilted axis cranking relativistic mean-field theory [17] and via geometrical model in Ref. [18]. Along with the  $^{60}\text{Ni}$ [14], the magnetic rotational band has also been reported in  $^{62}\text{Co}$ [19]. For both the nuclei, the occupation of proton hole in the high- $j$   $\pi f_{7/2}$  and neutron particle in the  $\nu g_{9/2}$  orbital are described to form the shear arms. Recently, an adiabatic and configuration-fixed constrained triaxial CDFT calculations searched for the possible wobbling motions in  $^{59-63}\text{Ni}$  [20]. They predicted wobbling motion in  $^{59,61,62}\text{Ni}$ , specially for  $^{62}\text{Ni}$  they pointed out the Band D1 as the possible wobbling band involving  $\nu g_{9/2}^2$  configuration. Being in the same Fermi level for proton and neutron, the intermediate odd-mass  $^{61}\text{Ni}$  is emerged as an optimistic ground to search for the similar excitations. For  $^{61}\text{Ni}$  isotope, collective bands at high spins were not known according to the most recent study using the  $^{59}\text{Co}(^7\text{Li}, \alpha n)$  reaction in combination with a modern array of Ge detectors [16].

The aim of the present work is to populate high-spin states in  $^{61}\text{Ni}$  by using a heavy-ion induced reaction, and to search for possible collective excitations at high spins. Since it is difficult to reach high spin states in  $^{61}\text{Ni}$  with stable target-beam combinations, we selected the combination of a  $^{50}\text{Ti}$  target and a long-lived radioactive  $^{14}\text{C}$  beam.  $^{61}\text{Ni}$  was produced via the 3n-evaporation channel with a very high yield. Excited states in  $^{61}\text{Ni}$  were studied previously using the  $^{58}\text{Fe}(\alpha, n)$  and  $^{53}\text{Cr}(^{11}\text{B}, p2n)$  reactions [21, 22], and the  $^{48}\text{Ca}(^{18}\text{O}, 5n)$  reaction [23] where levels up to 5316 keV were identified, including a 799 keV transition depopulating the  $(17/2^+)$  level at 4818 keV to the  $15/2^+$  level at 4019 keV, which decays further mainly via a 593 keV transition to the  $13/2^-$  level at 3426 keV. In the most recent study [16], using the reaction  $^{59}\text{Co}(^7\text{Li}, \alpha n)$ , states were identified up to a possible spin of  $17/2^+$  at 6734 keV.

In the present work, based on the coincidences observed, a complex level scheme has been constructed reaching to about 13 MeV in excitation, including many newly observed transitions. New collective band structures of deformed and magnetic nature have been identified as will be discussed later which attracts attention to lifetime measurements in this nucleus in future experimental endeavours.

## II. EXPERIMENT

Excited states of  $^{61}\text{Ni}$  were populated using the  $^{50}\text{Ti}(^{14}\text{C}, 3n)$  fusion- evaporation reaction at 40 MeV incident energy at the John D. Fox Superconducting Accelerator Facility, Florida State University (FSU) with 10-12 nA

beam current on target. Based on the PACE IV calculations, the beam energy was chosen little higher than the energy with maximum possible cross section for  $^{61}\text{Ni}$  to populate the higher spin states. At 40 MeV beam energy, the 3n evaporation channel is found to be the most dominant channel with predicted cross section of 600 mb( 60% of total fusion cross section) with the p2n, 4n and  $\alpha$ -2n channels making up the rest. An isotopically enriched (90%) relatively thin  $^{50}\text{Ti}$  foil of  $500 \mu\text{g}/\text{cm}^2$  thickness was used as target to ensure that the recoils escape the target and emit  $\gamma$ -rays in flight. The  $\gamma$  energies were then Doppllar corrected to attain the precise energies of the various  $\gamma$ -transitions. The  $\gamma$  rays emitted from the excited states were detected using the FSU  $\gamma$ -ray array, consisting of six Clover type HPGe detectors and three single-crystal HPGe detectors. Four Clover detectors were placed at  $90^\circ$ , two Clovers are placed at  $135^\circ$  with respect to the beam direction. One single-crystal detector was placed at  $90^\circ$  while the other two single-crystal detectors were placed at  $45^\circ$  with respect to beam direction. Similar experimental conditions were also used and reported in our previous work [24, 25]. The pre-amplifier signals from the Clover detectors, single crystal HPGe, and BGO detectors were processed using a PIXIE based digital data acquisition system in 2 fold coincidence mode for the  $\gamma - \gamma$  coincidence measurements. The efficiency and energy calibrations of each detector were carried out using  $^{133}\text{Ba}$  and  $^{152}\text{Eu}$  standard radioactive sources, placed at the target position. The calibration and efficiency beyond the 1408 keV transition of  $^{152}\text{Eu}$  source were done by the high-energy transitions from  $^{56}\text{Co}$  source made at FSU using a proton beam.

## III. DATA ANALYSIS

The time stamped data were sorted using GNUS-COPE, a spectroscopic software package developed at FSU [26, 27]. A total of  $9.4 \times 10^4$   $\gamma - \gamma$  coincidence events have been accumulated from the present data. The event by event data were converted into a  $\gamma - \gamma$  coincidence matrix with 1.0 keV/channel dispersion, which was also converted to a Radware [28] compatible matrix to analyze the coincidences between the de-exciting  $\gamma$  rays. An asymmetric matrix was created using the data from the detectors at the backward ( $145^\circ$ ) angles on the y-axis and the data from the  $90^\circ$  angle detectors on the x-axis to find out the Directional Correlation from Oriented states (DCO) ratio [29] for various transitions. The Clover detectors at  $90^\circ$  were additionally used for the measurement of Integrated Polarization from Directional Correlation of Oriented states (IPDCO) [30, 31] for assigning parity to the excited states. The deduced DCO ratios and the IPDCO values were used to determine the multipolarities and the electric or magnetic nature of the transitions leading to  $J^\pi$  assignments of the states wherever possible.

The multipolarities of the transitions belonging to  $^{61}\text{Ni}$

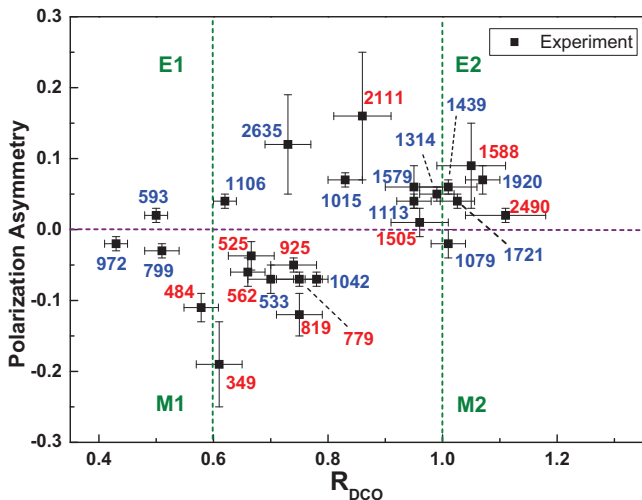


FIG. 1. DCO ratio vs polarization asymmetry ( $\Delta_{IPDCO}$ ) of some of the known (marked blue) and new transitions (marked red) in  $^{61}\text{Ni}$  obtained from different quadrupole gates. The dotted lines (green) parallel to the Y-axis correspond to the  $R_{DCO}$  values for dipole and quadrupole transitions in a pure quadrupole (E2) gate, respectively, and are shown to guide the eye. The dotted line (violet) parallel to the X-axis is to guide the eye for positive and negative values of  $\Delta_{IPDCO}$  for determining the electric and magnetic transitions, respectively.

were obtained from the DCO ratios ( $R_{DCO}$ ), defined by

$$R_{DCO} = \frac{I_{\gamma_1} \text{ at } \theta_1, \text{ gated by } \gamma_2 \text{ at } \theta_2}{I_{\gamma_1} \text{ at } \theta_2, \text{ gated by } \gamma_2 \text{ at } \theta_1} \quad (1)$$

The DCO ratio of an unknown ( $\gamma_1$ ) transition is obtained from the ratio of its intensities at two angles  $\theta_1$  ( $145^\circ$ ) and  $\theta_2$  ( $90^\circ$ ) gated by another transition ( $\gamma_2$ ) of known multipolarity, as per the equation 1. For the present experimental set-up, the typical value of  $R_{DCO}$  for a known quadrupole or dipole transition (for  $\gamma_1$ ) comes out to be 1.0 when gated by a transition of the same multipolarity ( $\gamma_2$ ). When gated by a known stretched and pure (mixing ratio  $\delta \approx 0$ ) quadrupole (dipole) transition ( $\gamma_2$ ), then the  $R_{DCO}$  value comes out to be close to 0.6 (1.7) for dipole (quadrupole) transition.

The parities of most of the excited states were determined by the polarization asymmetry measurement using the relative intensities of the parallel and perpendicular (with respect to the beam direction) Compton scattering of the emitted  $\gamma$  rays, detected in the corresponding crystals of the Clover HPGGe detector. The  $90^\circ$  detectors are used for this purpose to maximize the sensitivity of the polarization measurements ( $\Delta_{IPDCO}$ ) following the prescription of Ref. [30, 31].

The IPDCO asymmetry parameter ( $\Delta_{IPDCO}$ ) is defined as,

$$\Delta_{IPDCO} = \frac{a(E_\gamma)N_\perp - N_\parallel}{a(E_\gamma)N_\perp + N_\parallel} \quad (2)$$

where  $N_\parallel$  and  $N_\perp$  are the total counts of the  $\gamma$ -ray, scattered events in the planes parallel and perpendicular to the reaction plane, respectively. Here,  $a(E_\gamma) [= \frac{N_\parallel}{N_\perp}]$  is the geometrical correction factor (asymmetry factor) of the detector array and addresses the asymmetry in the response of the four crystals of a Clover Ge detector and was obtained from the known  $\gamma$  rays from  $^{152}\text{Eu}$  unpolarized source as a function of  $\gamma$ -ray energy. The values of  $a(E_\gamma)$  for different  $\gamma$ -ray energies are estimated from the fitting of the data points from the unpolarized source with a linear equation [ $a(E_\gamma) = a_0 + a_1 E_\gamma$ ] following the similar procedure described in Ref. [32] whereas the fit parameter are found to be  $a_0 = 0.96385$  and  $a_1 = 3.24 \times 10^{-5}$ . In order to calculate  $\Delta_{IPDCO}$ , the data were sorted to consider only the Compton events and two spectra were made with the total photopeak counts of parallel/perpendicular scattered events of the three  $90^\circ$  detectors. From these two parallel and perpendicular spectra, the number of counts in the perpendicular ( $N_\perp$ ) and parallel ( $N_\parallel$ ) scattering for a given  $\gamma$ -ray were obtained. The positive (negative) values of  $\Delta_{IPDCO}$  correspond to the electric (magnetic) transitions are listed in Table I for various transitions in  $^{61}\text{Ni}$ . The DCO ratio and the  $\Delta_{IPDCO}$  values of various known and new transitions are also shown in Fig. 1.

#### IV. RESULTS

The level scheme of  $^{61}\text{Ni}$  deduced from the present coincidence measurement is shown in Fig. 2 which is significantly extended up to a spin of  $35/2$  and excitation energy of 12874 keV with the observation of 76 new transitions and 28 new levels compared to the last published work [16]. All the low-lying known yrast and non-yrast states with the associated transitions, observed in the most recent high-spin study [16] were confirmed with a few exceptions. At higher spin, a sequence of 483 (484 keV in Fig. 2), 562 and 941 keV M1 transitions were reported in Ref. [16]. The presence of those transitions could be verified but they have been placed differently in the level scheme Fig. 2) according to the coincidence relationship from the present work. It has been noticed that apart from  $^{61}\text{Ni}$ , in the present experiment  $^{60}\text{Ni}$ ,  $^{59}\text{Ni}$ ,  $^{60}\text{Co}$  and  $^{59}\text{Co}$  also have been produced with little contamination. The present work reports the collective structure of  $^{61}\text{Ni}$  for the first time with the observation of four decay sequences referred as Bands B1, B2, B3 and B4 in Fig. 2 for the convenience of discussing them. Two of them, Bands B2 and B4 are build with the transitions of quadrupole (E2 in this case) nature whereas in the Bands B1 and B3 the states are connected by strong M1 transitions. The level scheme is formed based on the different coincidence relationships observed and relative intensities among the transitions. The spin-parity of the levels are determined from the measured  $R_{DCO}$  and  $\Delta_{IPDCO}$  values of the transitions. The details of the levels, and the  $\gamma$ -ray transitions measured in this work,



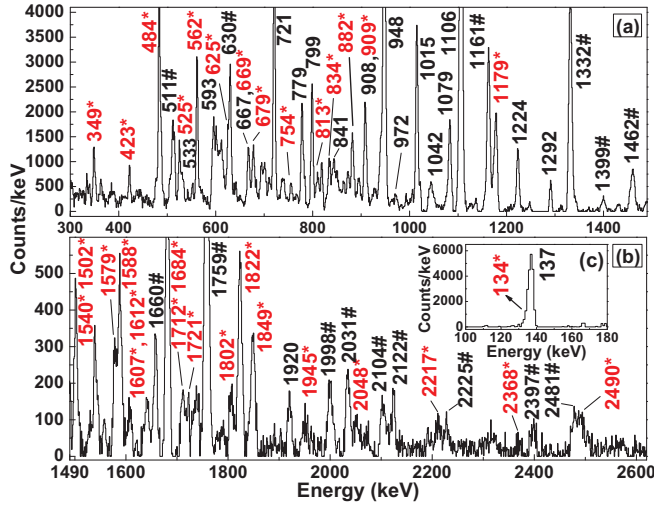


FIG. 3. Coincidence spectra gated by the 1177 keV transitions in  $^{61}\text{Ni}$ . The upper panel a (lower panel b) represents the  $\gamma$  transitions from 300 keV to 1490 keV (1490 keV to 2620 keV) range. The inset panel (c) shows the presence of the 134 and 137 keV transitions. ‘\*’ and red marked transitions are newly placed in the level scheme. The transitions marked with ‘#’ are the contamination from the neighbouring channels (mostly  $^{60}\text{Ni}$ ).

along with the DCO ratios and  $\Delta_{IPDCO}$  values for all the transitions in  $^{61}\text{Ni}$  are tabulated in Table I. The low-lying states, seen from the present work, are found to be of negative parity with a ground state of  $J^\pi = 3/2^-$ . The lowest opposite (positive) parity state  $9/2^+$  is observed at 2121 keV. The 1177 keV  $\gamma$  ray was reported to decay from  $11/2^+$  level at 3298 keV to the 2121 keV  $9/2^+$  spin state. The coincidence spectrum of the 1177 keV transition shown in Fig. 3 displays almost all  $\gamma$ -rays that were already known from prior work and are marked with black. Many new transitions are found to be present in this gate and marked with red (also \*) in the figure. Interestingly, the presence of an 1179 keV peak in the 1177 keV gate establishes that it is a doublet with the 1179-keV transition de-exciting from the level at 4477 keV. The absence of a 1314 keV transition in Fig. 3 also confirms that the new 1179 keV transition is decaying to the 3298 keV level bypassing the 3435 keV level. The inset of Fig. 3(c) shows the presence of 134 and 137 keV transitions. The presence of 1079 keV and 972 keV peak also confirms the placement of the 134 keV transition from the 2121 keV  $9/2^+$  state to the 1987 keV  $9/2^-$  state.

A representative coincidence spectrum for band B1 is shown in Fig. 4. This band is found to be connected to the already reported 4477 keV and 4206 keV levels with 670 and 941 keV connecting  $\gamma$ -transitions, respectively. The 384 keV transition is found to be in coincidence with the already known 2635 keV transition decaying from 4763 keV state and thus placed on the top of 4763 keV level. The DCO ratio and  $\Delta_{IPDCO}$  value of the 941 keV

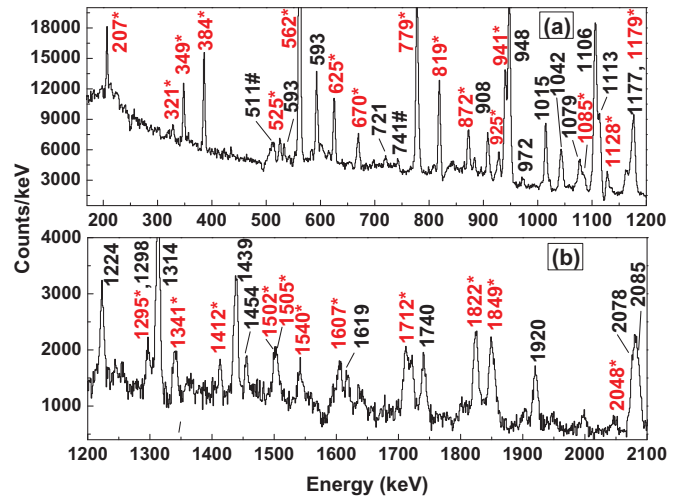


FIG. 4. Coincidence spectra gated by the 484 keV transition corresponding to band B1 in  $^{61}\text{Ni}$ . The upper panel a (lower panel b) represents the gamma transitions from 170 keV to 1200 keV (1200 keV to 2100 keV) range. All the M1 transitions corresponding to band B1 are shown along with the lower transitions. ‘\*’ and red marked transitions are newly placed in the level scheme. The transitions marked with ‘#’ are the contamination.

transition, as tabulated in Table I, confirms it to be of M1 nature and thus the spin and parity of the 5147 keV state is fixed as  $15/2^+$ . The Band B1 consists of M1 transitions, namely 384 keV, 562 keV, 779 keV up to the weak 1295 keV and can be seen from the figure along with the other new and known transitions from  $^{61}\text{Ni}$ . The DCO ratios and  $\Delta_{IPDCO}$  values of the transitions belonging to Band B1 are listed in Table I which established the magnetic dipole nature of the transitions. We have not identified any crossover E2 transitions for this band with the exception of one crossover transition, 1341 keV, that has been tentatively placed from the  $21/2^+$  to the  $17/2^+$  level. The spin-parity of the 5147 keV level is fixed as  $15/2^+$  from the M1 nature of 941 keV transition which is decaying from 5147 keV state to the known 4206 keV  $13/2^+$  state.

The band B2 is made up of a sequence of E2 transitions. The newly found transitions corresponding to Band B2 in coincidence with the 1588 keV (E2) transition are shown in Fig. 5. All the transitions (1179-, 1502-, 1540-, 1822- and 1945 keV) belonging to Band B2 can be seen in the 1588 keV gate. This band is connected to Band B3 with the 1963 keV transition also seen in 1588 keV coincidence gate. The regular pattern of E2 transitions starts from the 3298 keV level and extends up to the 12874 keV level with a plausible spin of  $35/2^+$ . The  $R_{DCO}$  and  $\Delta_{IPDCO}$  values confirm the spin and parity of the 4477 keV level as  $15/2^+$ . The positive parities of the states in Band B2 are confirmed from the nature of the 1588 and 1502 keV transitions. The DCO ratio values could not be found for the 1822 keV and 1945 keV

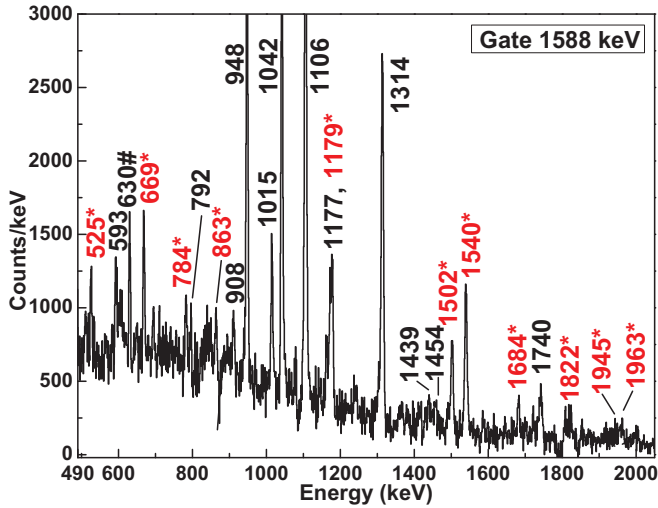


FIG. 5. Coincidence spectrum gated by 1588 keV showing the  $\gamma$  transitions corresponding to the transitions of band B2 in  $^{61}\text{Ni}$ . ‘\*’ and red marked transitions are newly placed in the level scheme. The transitions marked with ‘#’ are the contamination from the weakly populated neighbouring channels.

transitions due to limited statistics, therefore the spin-parity of the 10929 keV and 12874 keV levels are only tentatively assigned.

Another sequence of M1 transitions is found to be formed on top of the 7679 keV  $21/2^+$  level. The spin of this level is fixed from the quadruple nature of the 2523 keV transition which joins it to the already known 5156 keV level. The corresponding new transitions of band B3 are shown in the coincidence gate of the 349 keV transition in Fig. 6. The presence of 2048, 2368, 2523 and 2861 keV transitions in the 349-keV gate confirms the connection of Band B3 with band B2 and different single particle structures. This band extends up to 11138 keV level with the sequence 525, 784, 863 and 938 keV transitions on the top of the 349 keV transition, and these transitions show clear coincidences with the 349 keV transition (Fig. 6). The statistics corresponding to the 938 keV transition is limited and we could not determine the  $R_{DCO}$  or polarization asymmetry value for this transition. Thus the spin parity of the 11138 keV level is assigned as  $31/2^+$  tentatively.

The Band B4 in the level scheme of  $^{61}\text{Ni}$  is populated rather weakly upto higher spin. Two of its levels 3435 and 5156 keV were already known from the previous work connected through two E2 transitions 1721 and 1314 keV, respectively. The transitions belonging to Band B4 are confirmed by the coincidence with the 1721 keV transition, as shown in Fig. 7. This band is found to continue up to  $29/2^+$  10993 keV level with the sequence of 2111, 1684 and 2042 keV transition. The spin-parity of the  $21/2^+$  7267 keV level is confirmed from the E2 nature of 2111 keV level, whereas the spin of 8951 keV level is fixed as  $25/2$  from the  $R_{DCO}$  value of 2217 keV connected to the previously known  $21/2^+$  6734 keV level. Among

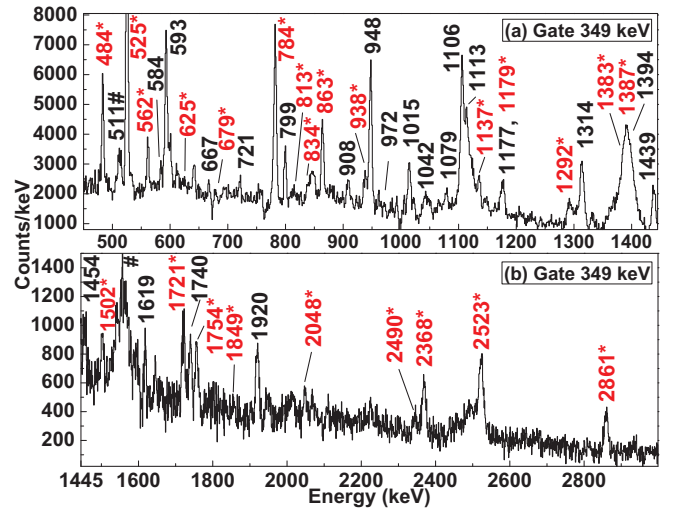


FIG. 6. Coincidence spectra gated by 349 keV showing the (a) lower energy from 450 keV to 1445 keV and (b) higher energy from 1445 keV to 2999 keV region corresponding to the transitions of band B3 in  $^{61}\text{Ni}$ . ‘\*’ and red marked transitions are newly placed in the level scheme. The transitions marked with ‘#’ are the contamination and the transitions from the neighbouring channels.

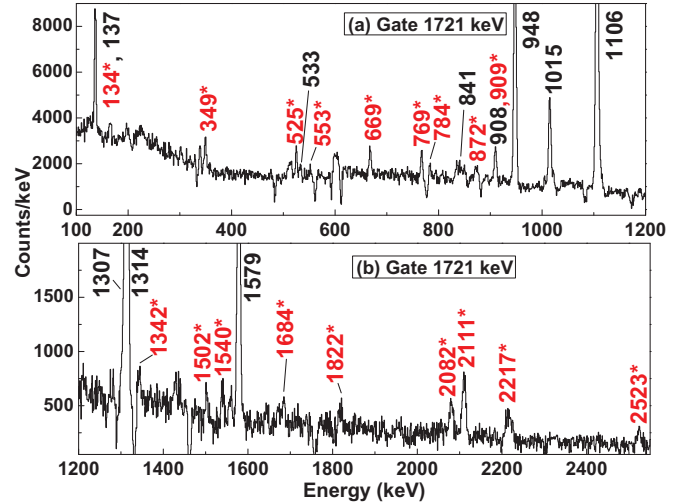


FIG. 7. Coincidence spectra gated by 1721 keV transition showing the (a) lower energy (100 to 1200 keV) and (b) higher energy (1200 to 2550 keV) transitions corresponding to the band B4 in  $^{61}\text{Ni}$ . ‘\*’ and red marked transitions are newly placed in the level scheme.

the three newly placed 2111, 1684, 2042 keV transitions in Band B4, the nature of the 2042 keV gamma cannot be confirmed because of overlapping with the already known 2045 keV transition, and thus the spin-parity of the 10993 keV level is tentatively assigned. The spin and parity of the band-head of Band B4 is taken as the positive parity  $9/2^+$ . This E2 sequence is found to be weakly populated after spin  $17/2^+$ .

## V. DISCUSSION

It is evident from the level scheme in Fig. 2 that with five valance neutrons outside the  $^{56}\text{Ni}$  doubly magic core,  $^{61}\text{Ni}$  is likely spherical at low spin and the lower excited irregular states are best described as single particle excitations. At higher spin, with more particle-hole excitations, collective behavior is expected and can be seen from several regular sequences in the level scheme.

### A. Low energy single particle structure and shell model calculations

The present work confirmed the already established low energy excited states from the previous studies on  $^{61}\text{Ni}$  as well as established many new negative and positive parity states which decay to those well known states. Since  $Ni$  has a magic proton number ( $Z=28$ ) and has only five neutrons outside the  $N=28$  shell, it is in the scope of the shell model calculations to interpret its low energy structures. To reproduce the experimental low energy states we used Shell Model (SM) calculations involving available orbitals near the Fermi surface. It has been seen that in the mass region  $Z$  or  $N$  from 20 to 40, natural parity states for odd(even) mass nuclei with  $\pi=-(+)$  can be described well within  $fp$ -shell model space with a inert core of  $^{40}\text{Ca}$ . Therefore, for the low lying negative parity states, the shell model involves the  $2p_{3/2}$ ,  $0f_{5/2}$  and  $2p_{1/2}$  shells above the  $N$ ,  $Z=28$  gap and the  $0f_{7/2}$  shell below the gap. However, to explain the unnatural parity state with  $\pi=+(-)$  for the odd (even) mass nuclei in this region, the model space within the major  $fp$  shell is not enough. Thus in the present calculation, to interpret the higher lying positive parity states in odd mass  $^{61}\text{Ni}$  the inclusion of  $0\nu g_{9/2}$  and  $1\nu d_{5/2}$  is necessary along with the major  $fp$  shell. The present shell model calculation is carried out using the  $\text{GXPF1Br}+V_{MU}$ (modified) interaction and the model space is composed of  $(0f_{7/2}+2p_{3/2}+0f_{5/2}+2p_{1/2})+\nu g_{9/2} + \nu d_{5/2}$  orbitals [33]. The configuration space was truncated to allow up to six-particle excitations, from the  $0f_{7/2}$  shell to the upper  $fp$ -shell for protons. In the case of neutrons, to focus on the states dominated by the  $1p-1h$  positive parity states across the  $N=40$  shell gap, only one neutron is allowed to occupy the  $0g_{9/2}$  or  $1d_{5/2}$  orbitals.

The low-lying experimental negative parity and positive parity states are compared with the SM generated states in Fig. 8(a) and Fig. 8(b) respectively. The difference between the SM calculated states and the experimental levels are also shown at the bottom of each figure. It is observed that both for positive parity and negative parity, the first experimental excited state of each spin that is the so called yrast states are matched quite well with the shell model predictions. The SM generated negative parity states are predicted to have the proton mostly paired to spin 0 and the configuration of these states can be described as the odd neutron(s) occu-

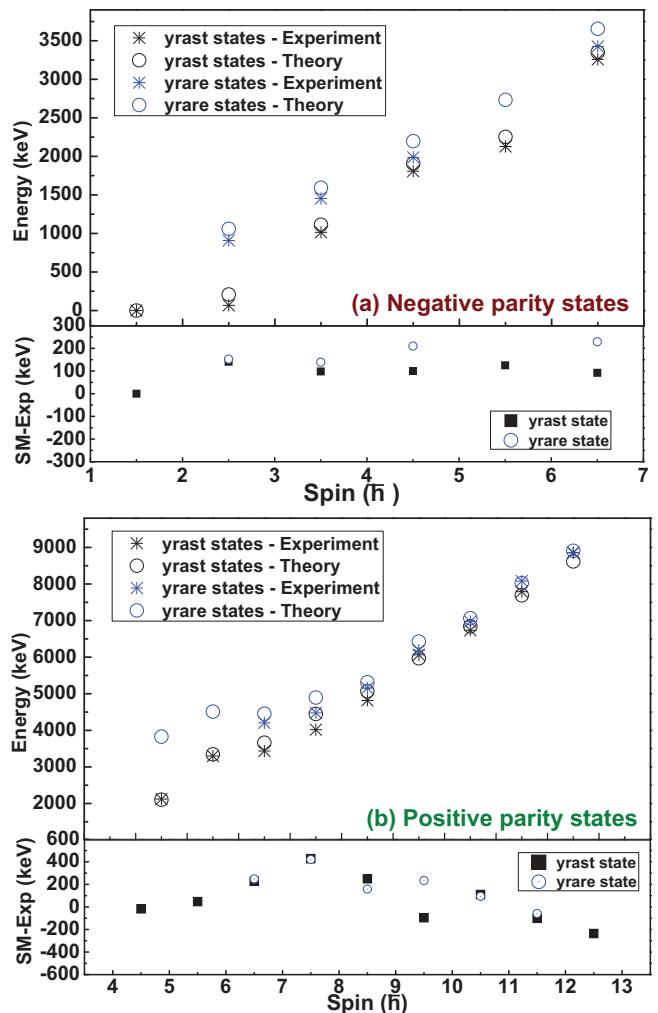


FIG. 8. The excitation energies of (a) negative parity and (b) positive parity low lying experimental states with SM calculations using the  $\text{GXPF1Br}+V_{MU}$ (modified) interaction and the difference of the energies between SM calculated states and experimental levels. The first (yrast) and second excited (yrare) states for both experimental and theoretical levels of each spin are plotted. The experimental energy levels are marked with '\*' whereas the SM calculated states are represented with open circles. The difference between the SM and experimental levels for yrast states and yrare states are represented as solid box and open circle, respectively. The negative parity states are well reproduced using the  $\nu p_{3/2}$ ,  $\nu f_{5/2}$  and  $\nu p_{1/2}$  orbitals, whereas for all the positive parity states, the neutrons are allowed to occupy the  $\nu g_{9/2}$  or  $\nu d_{5/2}$  orbitals.

pying the  $\nu p_{3/2}$ ,  $\nu f_{5/2}$  or  $\nu p_{1/2}$ . The experimental yrare state for  $1/2^-$  and  $11/2^-$  spin have not been observed in the present data.

On the other hand for the positive parity states, SM calculation shows that a neutron has to be excited into the positive parity  $\nu 0g_{9/2}$  orbital. The first three SM predicted yrast states match reasonably well with the experimental yrast states. It may also be noted that we haven't seen any experimental yrare state for  $9/2^+$

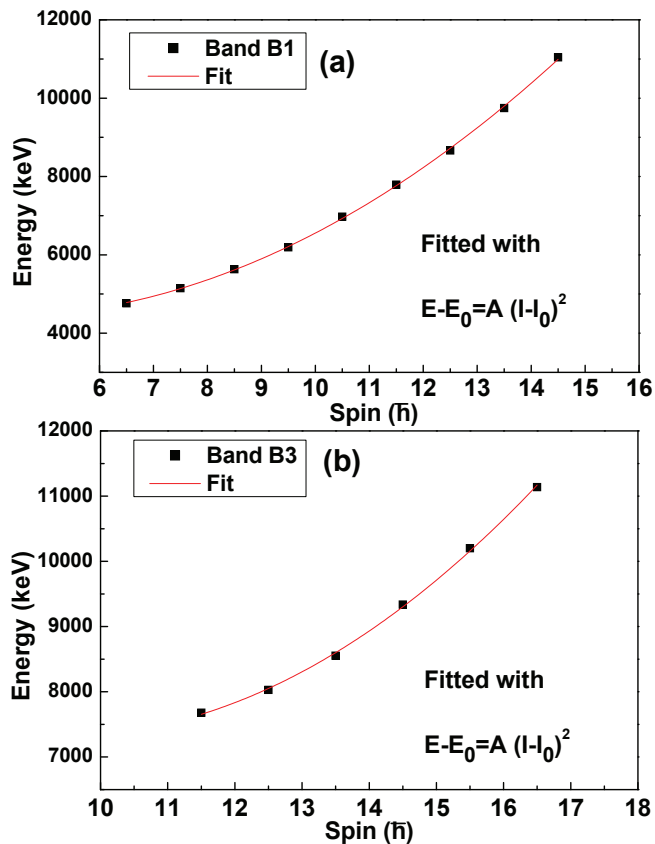


FIG. 9. The excitation energy of (a) Band B1 and (b) Band B3 as a function of the spin of the level. The experimental data are fitted with Eq. 3 where  $E_0$  and  $I_0$  represent the band head energy and spin respectively.

and  $11/2^+$  spin. Beyond those two spins, the yrast and yrare states are coming closer in energy as the spin increases. This is expected as with more energy and spin, more and more orbitals are accessible by the neutrons and protons for which the density of states are increasing significantly. Here it is worth mentioning that the yrast  $9/2^+$  and  $13/2^+$  states are part of the Band B4 and the SM calculation well reproduces those states of the Band B4 along with the other collective bands which will be discussed later.

### B. Bands B1 and B3

In the present work we have found two regular sequence of M1 transitions, named Bands B1 and B3, marked in Fig. 2. Both are comprised of states with positive parity. The involvement of the  $\nu 0g_{9/2}$  orbital plays a crucial role in the structure of these bands. To understand the nature of these bands, excitation energy as a function of spin has been plotted in Fig 9. The excitation energy for both M1 sequences have been fitted with Eq. 3 to understand their rotational nature.

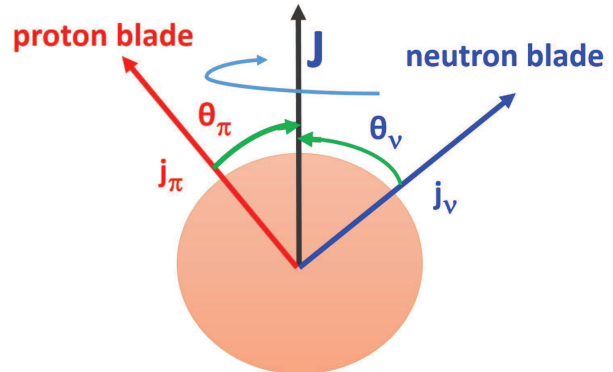


FIG. 10. The orientation of proton (particle/hole) and neutron (hole/particle) angular momenta vectors with respect to the core angular momentum in the case of shears bands. With energy, the two angular momentum vectors (the arms of the shear closes down) align themselves with the core angular momentum due to interaction between the two angular momentum vectors.

$$E - E_0 = A * (I - I_0)^2 \quad (3)$$

where  $E_0$  and  $I_0$  represents the band head energy and spin respectively and  $A$  is an arbitrary parameter.

It is evident from Fig 9 that the Eq. 3 fits the experimental data quite well for both the bands. Therefore, it can be said that the excitation energy of these two bands follows the trend of a rotational band. For further investigation, these two sequences of magnetic dipole transitions have been studied in the framework of SCM description of shears mechanism [34] prescribed by Machiavelli and Clark [35–37].

#### 1. Magnetic rotational band and shears mechanism

Observation of rotational-like strong sequence of magnetic dipole (M1) transitions with very weak or no crossover E2 transitions in nearly spherical nuclei are often found to be generated from shears mechanism and well known as magnetic rotational (MR) bands. This MR band structure is generated due to the symmetry breaking by the associated magnetic moments of the current of few high-spin hole and particles outside a weakly deformed core. As these magnetic moments break the symmetry of the system and rotate around the total angular momentum of the near spherical core, this mode of nuclear excitations is described as magnetic rotational band [34, 35, 38, 39].

This type of sequence exhibits some special features like a strong  $B(M1)$  strength and a small  $B(E2)$  value,

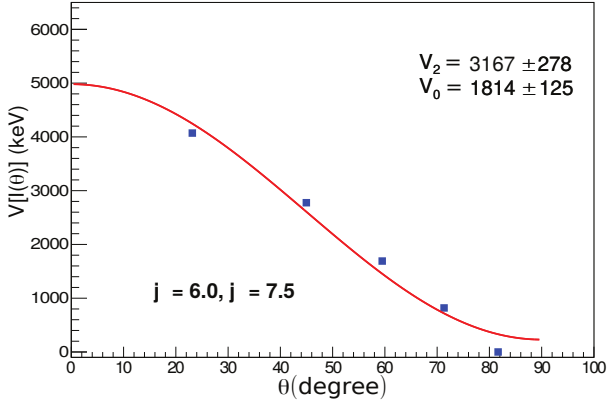


FIG. 11. SCM fit with the experimental data for magnetic rotational band B1.

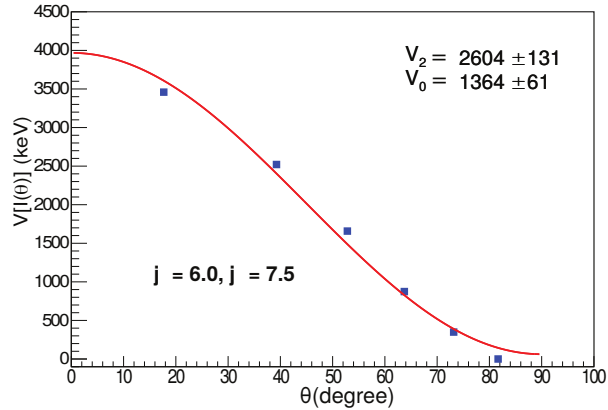


FIG. 12. SCM fit with the experimental data for magnetic rotational band B3.

resulting in a large  $B(M1)/B(E2)$  value. The current distributions of a few high spin particles and holes outside a near spherical core breaks the symmetry, resulting in these types of strong M1 sequences. The magnetic moments associated with these currents rotates around the total angular momentum vector. At the band head, the magnetic rotational band starts with a  $90^\circ$  angle between the two shear arms formed with particle and hole angular momentum. With increasing excitation energy the two arms come closer and align themselves with the angular momentum of the core, increasing the total angular momentum of the system. At the highest point of the band the particle and hole angular momentum is completely aligned and the angle between the two arms approaches zero.

The shear structure were first described by Frauendorf using the tilted-axis-cranking model [34], and a semi-classical model (SCM) was described by Macchiavelli et al. [36]. The SCM describes schematically how the energy states of a shears band are generated from the coupling

of long spin vector of proton particles(or holes)  $j_\pi$  and neutron holes(or particles)  $j_\nu$ . The shears angle  $\theta(I)$  ( $= \theta_\pi + \theta_\nu$ ), i.e. the angle between two long spin vectors  $j_\pi$  and  $j_\nu$  as shown in Fig. 10, is a function of total spin ( $I$ ) and for a given angular momentum state (of total spin  $I$ ), it can be derived semiclassically using the expression

$$\cos[\theta(I)] = \frac{\vec{j}_\pi \cdot \vec{j}_\nu}{|\vec{j}_\pi| |\vec{j}_\nu|} = \frac{I(I+1) - j_\pi(j_\pi+1) - j_\nu(j_\nu+1)}{2\sqrt{(j_\pi(j_\pi+1)j_\nu(j_\nu+1))}} \quad (4)$$

The  $j_\pi$  and  $j_\nu$  are chosen to reproduce the band-head spin. For a nucleus with small deformation, it has been observed that the total angular momentum has some contribution from the collective core in addition to that from the shears mechanism. Therefore, the total angular momentum can be written as  $\vec{I} = \vec{I}_{Sh} + \vec{R}_{core}$  where the  $R_{core}$  represent the core angular momentum. The small effect of the core towards the total angular momentum is represented by,

$$R_{core} = \left(\frac{\Delta R}{\Delta I}\right) * (I - I_{bh}) \quad (5)$$

Using the band head spin  $I_{bh}$ ,  $j_\pi$ ,  $j_\nu$  and the maximum spin observed in a band  $I_{max}$  the  $\Delta R$  and  $\Delta I$  can be estimated as  $\Delta R = I_{max} - (j_\pi + j_\nu)$  and  $\Delta I = I_{max} - I_{bh} = I_{max} - \sqrt{j_\pi^2 + j_\nu^2}$  which leads to

$$\frac{\Delta R}{\Delta I} = \frac{(I_{max} - (j_\pi + j_\nu))}{(I_{max} - \sqrt{j_\pi^2 + j_\nu^2})} \quad (6)$$

Because of the effective interaction  $V[I(\theta)]$  between the proton and neutron angular momenta, dynamics of the system gives rise to a rotation like spectrum consisting M1 transitions. The effective interaction  $V[I(\theta)]$  can be represented in terms of an expansion of even multipoles as stated in [36]

$$V[I(\theta)] = V_0 + V_2 \frac{3\cos^2\theta - 1}{2} + \dots \quad (7)$$

The excitation energies along the MR band are generated due to the effective interaction by re-coupling of the two long angular momentum vector and can be calculated from the experimental energy level of the band as  $V[I(\theta)] = E(I) - E_{bh}$ .

With the aim to extract the effective interaction ( $V_2$ ) between the nucleons involved in generation of angular momentum by the shears mechanism for the different bands, we plot the  $E(I) - E_{bh}$  (i.e  $V[I(\theta)]$ ) vs the shears angle  $\theta(I)$  for band B1 and B3 using the above formalism and fit it with Eq. 7 assuming the probable  $j_\pi$  and  $j_\nu$ .

In  $^{60}\text{Ni}$  the negative parity magnetic rotational bands (marked as M1 and M4 in ref. [14]) are predicted to have the configuration  $\pi(f_{7/2}^{-1}(fp)^1) \otimes \nu(g_{9/2}^1(fp)^3)$ . Considering the similar configuration for the dipole band B1 and B3 in  $^{61}\text{Ni}$ , the experimental data are fitted with the Eq. 7. The proton (hole) and neutron(particle) angular

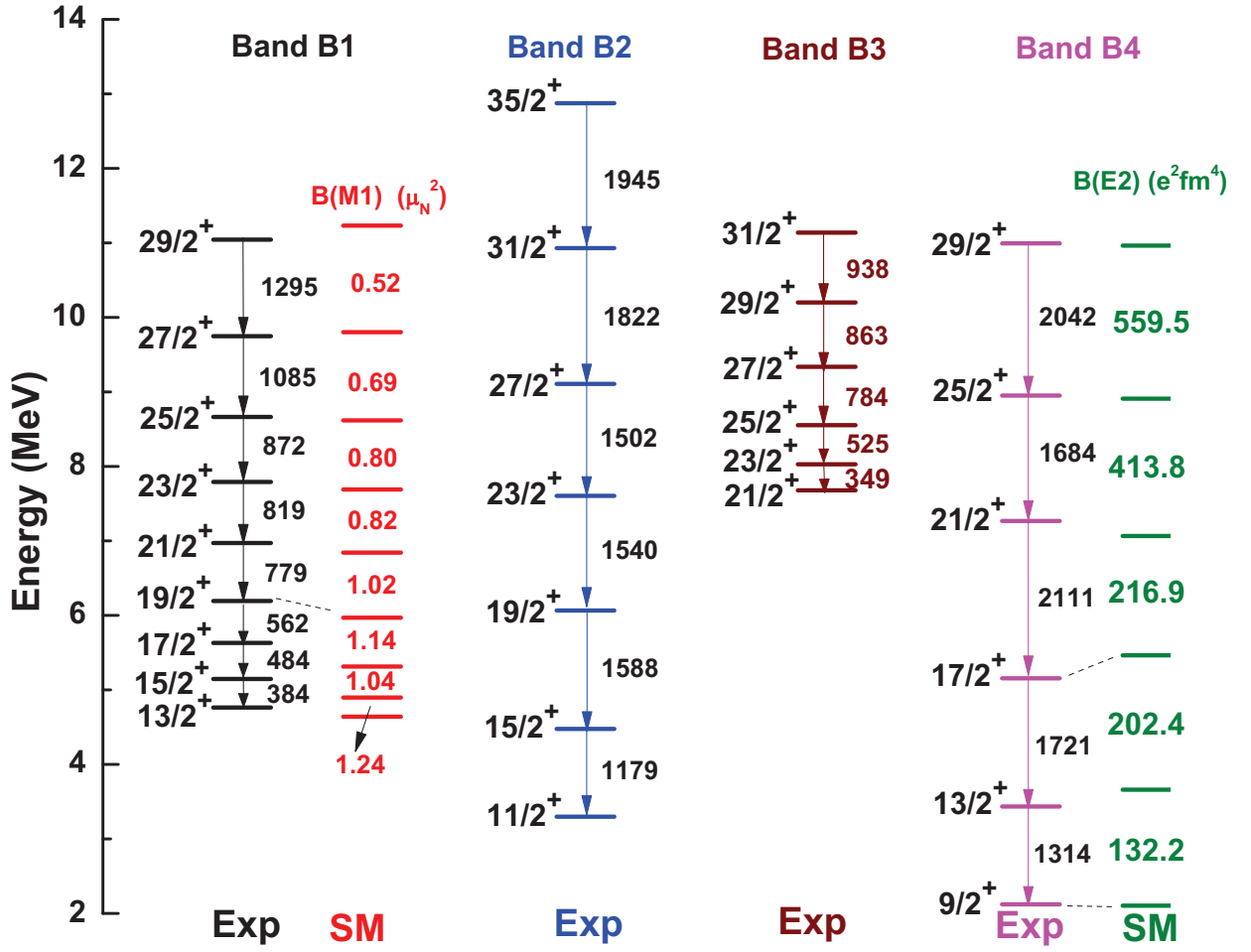


FIG. 13. Simplified level structure of  $^{61}\text{Ni}$  showing the four collective structures newly found in the present work. The shell model calculated levels (right panel) along with the experimental levels (left panel) are shown for Band B1 and B4 for comparison. The shell model calculations were done with the GXPF1Br+ $V_{MV}$  (modified) interaction using the model space composed of  $(0f_{7/2}+2p_{3/2}+0f_{5/2}+2p_{1/2})+\nu g_{9/2}+\nu d_{5/2}$  orbitals both for proton and neutron with the truncation of  $1p-1h$  states. The spins of each levels are marked for each band. The dashed lines from the experimental levels to the SM calculated levels are to indicate corresponding spin states of each band. For each SM calculated level, the  $B(M1)$  values (for Band B1) and  $B(E2)$  values (for Band B4) are shown in the gap between the corresponding states. For the experiment, the arrows indicate the  $\gamma$  transitions and the energies (in keV) are also noted alongside.

momentum ( $j_\pi$  and  $j_\nu$ ) corresponding to the blades of the shear are chosen so as to have the shears angle nearly  $90^\circ$  at the band head energy as well as to generate the spin throughout the band by the gradual alignment of these two angular momenta. Depending on the configuration suggested in ref. [14], if we consider the  $j_\pi$  and  $j_\nu$  as  $6\hbar$  and  $7.5\hbar$  respectively for Band B1, for the first few spin states upto  $19/2^+\hbar$  the shears angle is found to be more than  $90^\circ$ . Thus the band head energy and the spin for Band B1 is considered as 6972 keV and  $21/2^+$  to plot the  $V[I(\theta)]$  as a function of shears angle  $\theta$  in Fig. 11. The SCM model fit using Eq. 7 matches quite well with the experimental data with the above considerations for the upper part of Band B1. The effective interaction strength  $V_2=3167$  keV from the fit in Fig. 11 seems to match with the effective interaction of the magnetic rotational band

reported in the neighbouring  $^{60}\text{Ni}$  [18]. The shears angle is found to be about  $90^\circ$  for the  $21/2^+$  spin state and reaches about  $25^\circ$  at the maximum observable spin ( $29/2^+$ ) level for Band B1. For the first few states making up band B1, it seems there is less contribution from the  $j_\pi$  and  $j_\nu$  for the shears mechanism and therefore the geometrical model does not agree well for these states using  $j_\pi = 6\hbar$  and  $j_\nu = 7.5\hbar$ .

For Band B3, same values of  $j_\pi$  and  $j_\nu$  are considered ( $j_\pi=6\hbar$  and  $j_\nu=7.5\hbar$ ) to fit the experimental data. The Eq. 7 fitted the experimental data quite well for Band B3 as can be seen from Fig. 12 considering the band head energy and spin of the Band B3 as 7679 keV and  $21/2^+$  respectively. The interaction strength is found to be  $V_2=2604$  keV which is a bit less compared to that of Band B1. It is seen from the Fig. 12 that the shears angle

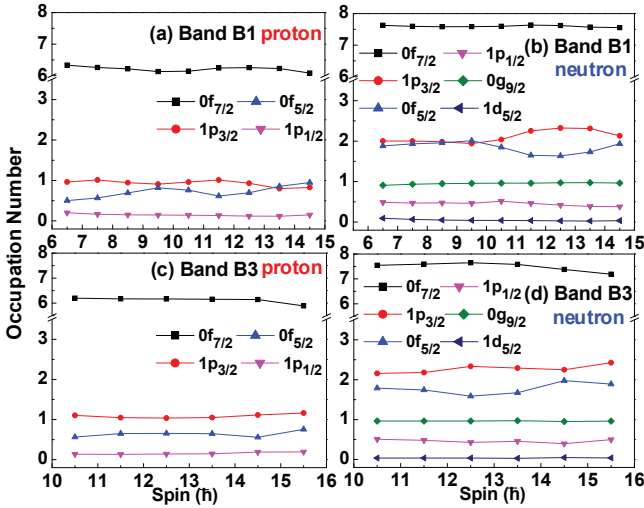


FIG. 14. The occupation number for different orbitals calculated by shell model calculation with respect to spins of the levels. The upper panel is consisting of the occupation number for (a) proton and (b) neutron associated with Band B1 configuration whereas the lower panel shows occupation number associated with the Band B3 configuration for (c) proton and (d) neutron.

$\theta$  is about  $90^\circ$  at the band head and gradually approaches  $15^\circ$  at the highest spin. The Fermi surface of the proton-hole is near the  $\pi f_{7/2}$  orbital in this nucleus and that for the neutron particles, it is near the  $\nu g_{9/2}$  orbital. The proton holes in the high-j  $f_{7/2}$  and neutron particle in the high-j  $g_{9/2}$  orbital mainly build the two angular momenta arms of the shears bands discussed above. We find that the same value of  $j_\pi$  and  $j_\nu$  fits well for both the MR bands in  $^{61}\text{Ni}$  similar to what was observed for the configuration of the two negative parity magnetic rotational bands (M1 and M4 in Ref. [14]) in  $^{60}\text{Ni}$ . Further, We have tried to identify the corresponding states of Band B1 and B3 from the SM calculations to understand their intrinsic structure as discussed in the next section.

## 2. Magnetic dipole band and Shell Model Calculation

The positive parity states corresponding to the band B1 can be reproduced within the scope of the SM calculation as discussed before. The states which form the magnetic rotational bands are identified by their higher transition ( $B(M1)$  values) probabilities associated with them. The experimental levels and Shell Model predicted states are compared in Fig. 13 for Band B1 and a good agreement is observed. The comparatively large SM calculated  $B(M1)$  values are also shown in the corresponding gap of SM calculated states in Fig. 13, which represent a nice decreasing trend with spin. Therefore, the important criteria of shears mechanism of having decreasing  $B(M1)$  values across the band with the closing of two shears arms is well reproduced with the SM calculation. To un-

derstand the configuration of the bands, the occupation number of different orbitals for Band B1 (and also Band B3) are plotted as a function of spin and shown in the Fig. 14. For neutron, the occupation number for band B1 clearly indicates that one neutron occupies the  $g_{9/2}$  orbital whereas all the other four neutrons reside in the  $fp$  shell. If we follow the trend of the occupation number for  $1p_{3/2}$  and  $0f_{5/2}$  orbitals with spin, we can see that there is a gradual change in occupancy especially after  $19/2^+$  spin which is consistent with the geometrical model interpretation of Band B1. It may happen that only after  $19/2^+$  spin, the neutrons are completely aligned and then the shears arms formed by the protons and neutrons start closing to generate the higher spin. The shell model picture also supports the choice of the band head at  $21/2^+$  in Fig. 11 and the high  $j_\nu$  value as used in the geometrical model is also justified. Along with that, one have to keep in mind that the expected (favourable)  $90^\circ$  angle between the proton and neutron arm at the band head in the shears mechanism is based on the argument that protons are in pure hole states and neutrons are in pure particle states (or vice versa). For  $^{61}\text{Ni}$ , on the other hand, proton angular momentum is created by  $\pi(f_{7/2}^{-1}f_{5/2}^1)$  configuration, which is a mixture of hole and particle state. This may change the favorable angle between these two arms and the angle can be more than  $90^\circ$  at the band head. Another important note to be made about the occupation number is that it can have contribution from the pairing correlation. With both proton hole and neutron particle in high-j orbital, the ideal situation of creating a shears band exists and the high  $B(M1)$  values from the shell model calculations strengthen the concept of a magnetic rotational band. Therefore, from the occupation of protons and neutrons in different orbitals, the upper part of Band B1 are predicted to have the configuration  $\pi(f_{7/2}^{-1}[p_{3/2}/f_{5/2}]^1) \otimes \nu(g_{9/2}^1 p_{3/2}^2 [f_{5/2}/p_{1/2}]^2)$  and they agree with the configuration proposed in  $^{60}\text{Ni}$  Band M1 as well.

The SM predicted energies for the Band B3 are a little bit over-estimated compared to the experimental data and therefore are not show in Fig. 13. To understand the structure of Band B3, the neutron occupation numbers for various orbitals are compared to Band B1 in Fig.14(b) and (c). It may be worth mentioning that unlike the Band B1, the occupation number for neutron for Band B3 remains same for the entire spin range and matches with the later part of Band B1. Therefore, from the SM calculation, the configuration for band B3 is predicted to be similar as Band B1 if not same. This configuration of Band B3 also supports the choice of same  $j_\pi$  and  $j_\nu$  values corresponding to the geometrical semi-classical model fit with respect to Band B1, as discussed in previous section.

## C. Bands B2 and B4

We have observed two more sequences connected by E2 transitions indicated as Band B2 and Band B4 in Fig. 2.

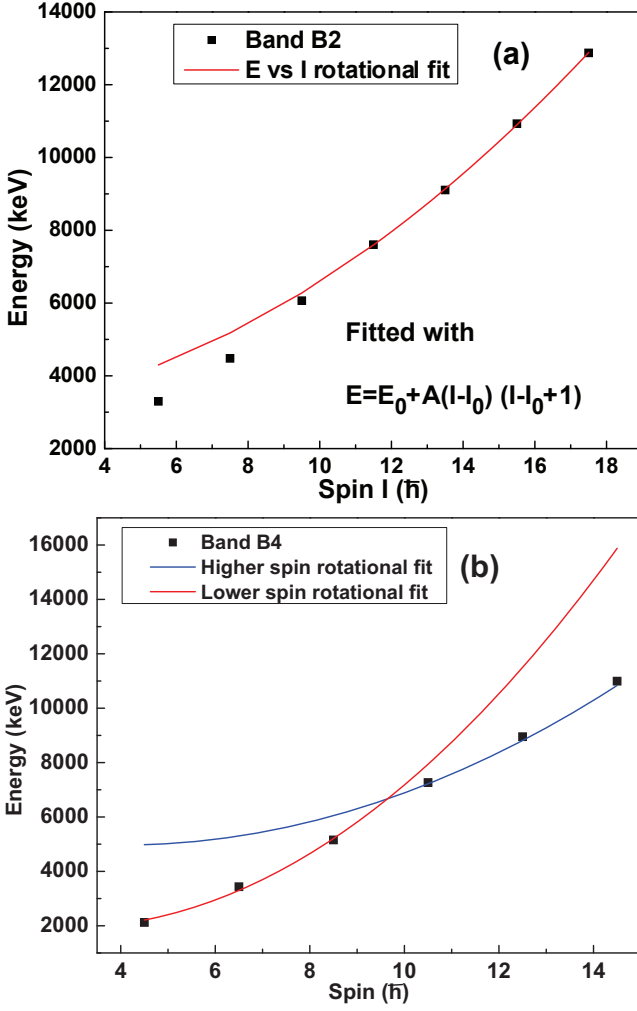


FIG. 15. The excitation energy of (a) Band B2 and (b) Band B4 as a function of the spin of the level. The experimental data are fitted with Eq.  $E = E_0 + A * (I - I_0)(I - I_0 + 1)$ , where  $A$ ,  $E_0$  and  $I_0$  are varied as free parameter.  $E_0$  and  $I_0$  are equivalent to the band head energy and spin respectively for the corresponding Band (Band B2 and B4).

The Band B4 starts right from the first observed  $9/2^+$  spin and extends upto  $29/2^+$  whereas the band B4 is assumed to start from  $11/2^+$  spin. It is quite clear that the involvement of the shape-driving  $g_{9/2}$  orbital induces deformation and the rotational bands are likely to be seen as also reported in neighbouring nuclei. To find out the nature of these two bands we plot the excitation energy vs spin for both the bands (B2 and B4) which are displayed in Fig. 15(a) and (b). The trend in the E vs I plot for Band B2 suggests that the first few transitions are not a part of the rotational structure, whereas the transitions beyond the  $23/2^+$  spin can be fitted with the rotational equation described as

$$E = E_0 + A * (I - I_0)(I - I_0 + 1) \quad (8)$$

The experimental data in Fig. 15 for both the bands are fitted with Eq. 8. For Band B2, the fitting is for the

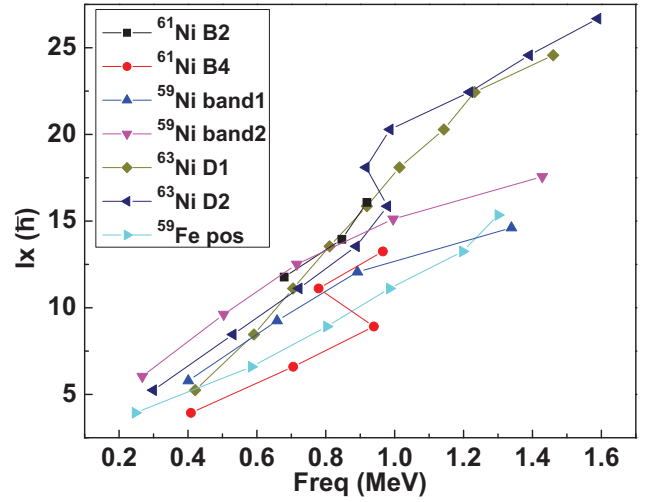


FIG. 16. The aligned angular momentum of Band B2 and Band B4 of  $^{61}\text{Ni}$  comparing with the rotational bands reported in neighbouring odd mass  $Ni$  isotopes and  $^{59}\text{Fe}$  as a function of the rotational frequency ( $\hbar\omega$ ) of the levels. The information of the excited levels for  $^{59}\text{Ni}$ ,  $^{63}\text{Ni}$  and  $^{59}\text{Fe}$  are taken from the Ref. [13], [15] and [40] respectively.

upper 4 data points starting from  $23/2^+$  and clearly, this rotational structure is not followed by the states below  $23/2^+$  spin. For band B4, the E vs I plot indicates the overlap of two sequences. Therefore they are fitted by the rotational equation in two part: lower energy part and higher energy part, which is shown in Fig. 15(b). The fitted curves indicate the crossing of two rotational bands around  $23/2^+$  spin. The fitted parameter  $A$  in Eq. 8 is inversely proportional to the Moment of Inertia (MoI) of the nuclear shape of associated with the corresponding band. The values obtained for  $A$  for Band B2 (upper part) (Fig. 15(a)) and Band B4 lower and upper part (Fig. 15(b)) are 28, 103 and 53 respectively. Therefore, the higher slope of Band B4 compared to Band B2 indicates that a higher moment of inertia is associated with the Band B2 rotational structure. Thus the configuration for band B4 can be assumed to have less number of quasi-particle involving one  $\nu 0g_{9/2}$  orbital and possibly the upper part of Band B4 may have more quasi-particles.

To understand the structure better, the aligned angular momentum ( $I_x$ ) for bands B2 and B4, observed in  $^{61}\text{Ni}$  from the present work are compared with the similar rotational bands reported in neighbouring  $Ni$  and  $Fe$  nuclei and are shown in Fig. 16. As the Band B4 starts from the very first observed  $9/2^+$  state, the configuration  $\pi(f_{7/2}^{-1}(fp)^1) \otimes \nu(g_{9/2}^1(fp)^4)$  is assumed for the lower part of the Band B4. As the aligned angular momentum is low for the first part of the band B4, we can assume that the few neutrons in  $fp$  shell are paired up and do not contribute to the total angular momentum. The aligned angular momentum ( $I_x$ ) for the lower part of the Band B4 are matched with those of the positive parity band of  $^{59}\text{Fe}$

with only two proton less than  $^{61}\text{Ni}$ . Band B4 is seen to exhibit a back-bending at 0.95 MeV rotational frequency (around spin  $10.5\hbar$ ) and seems to have a different intrinsic structure after  $21/2^+$  spin. With only two more neutron compared to  $^{59}\text{Ni}$ , the rotational bands of  $^{61}\text{Ni}$  are expected to have similar kind of structure as the rotational bands reported in  $^{59}\text{Ni}$ . The configuration of rotational Band 1 of  $^{59}\text{Ni}$  is predicted to be  $\pi(f_{7/2}^{-2}(p_{3/2}/f_{5/2})^2) \otimes \nu((p_{3/2}f_{5/2})^2g_{9/2}^1)$  from configuration-dependent cranked Nilsson-Strutinsky (CNS) calculations [13]. The Band B4 is not well extended after the band crossing, but the  $I_x$  of the Band B4 after band crossing has the indication to match well with that of Band 1 of  $^{59}\text{Ni}$  and thus the upper part of Band B4 is proposed to be generated from promoting an extra proton to the upper  $fp$  shell and creating an extra hole in high- $j$   $f_{7/2}$  which in turns increase the angular momentum of the system. The aligned angular momentum also supports the configuration of  $\pi(f_{7/2}^{-2}(fp)^2) \otimes \nu(g_{9/2}^1(fp)^4)$  for band B4 after the back-bending. The deformation for the configuration involving the  $\nu g_{9/2}^1$  orbital in  $^{61}\text{Ni}$  is predicted to be  $\beta_2=0.24$  from configuration-fixed constrained CDFT calculations in Ref. [20]. Therefore we can also assume the same deformation for the upper part of Band B4. The configuration-dependent cranked Nilsson-Strutinsky (CNS) approach also predicts a similar deformation ( $\epsilon_2=0.22$ ) for the collective band WD1 in  $^{60}\text{Ni}$  [14] with the configuration  $\pi(f_{7/2}^{-2}(fp)^2) \otimes \nu(g_{9/2}^1(fp)^3)$ . Therefore the deformation of Band B4 is assumed to be of the same order as predicted in Ref. [20].

The  $I_x$  for the upper part of Band B2 in  $^{61}\text{Ni}$  is only plotted in Fig. 16 as the states below  $23/2^+$  are not a part of the rotational structure. The  $I_x$  of the Band B2 seems to have relatively higher values with respect to Band B4 and matched with the lower part of the D1 band of  $^{63}\text{Ni}$  [15] as well as with band 2 of  $^{59}\text{Ni}$ . The positive parity Band D1 of  $^{63}\text{Ni}$  is predicted to have the configuration involving  $\pi g_{9/2}$  and  $\nu g_{9/2}^2$  to generate such large aligned angular momentum. Similarly, the band 2 of  $^{59}\text{Ni}$  is also predicted to have both  $\pi g_{9/2}^2$  and  $\nu g_{9/2}^1$  orbitals involved in the configuration. It may be noted that these bands in  $^{59}\text{Ni}$  or  $^{63}\text{Ni}$  appear at a higher excitation energy. From the present experimental data, we could not extend the Band B2 beyond  $35/2^+$  and thus it is difficult to predict the intrinsic structure for this band. But it may be inferred that the configuration related to Band B4 involve more high- $j$  orbital(s) along with one  $\nu g_{9/2}$  in it.

### 1. Shell Model Calculations for Band 2 and 4

The experimental states corresponding to the rotational Band B4 are also compared with the SM calculated states and shown in Fig. 13. The SM calculation for Band B4 matched beautifully with the experimental value. This band is predicted to have a high  $B(E2)$  val-

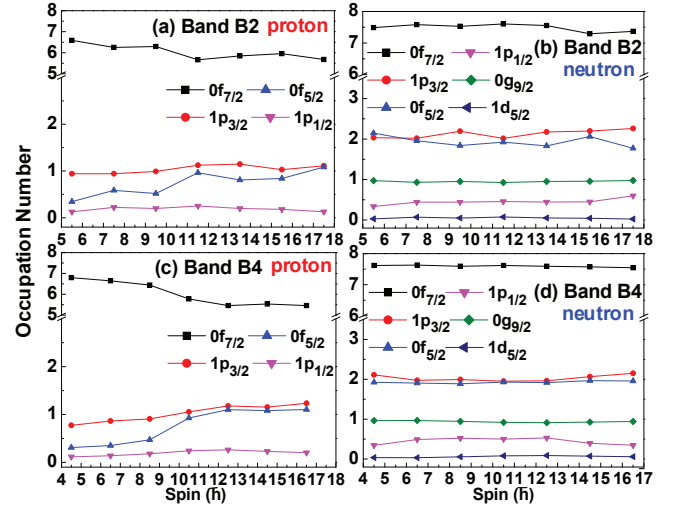


FIG. 17. The occupation number for different orbitals calculated by shell model calculation with respect to spins of the levels. The upper panel shows the occupation numbers for (a) proton and (b) neutron associated with Band B2 configuration whereas the lower panel shows occupation number associated with the Band B4 configuration for (c) proton and (d) neutron.

ues (in order of  $200 \text{ e}^2 \text{ fm}^4$ ) for the lower states which increase even higher after  $21/2^+$  spin. The occupation number for both the Band B2 and B4 are represented in Fig. 17 calculated by the SM using same prescription described above. As these bands (Band B2 and B4) are associated with some deformation, the spherical orbital configuration are not so rigid. The occupation number for the Band B4 predicts one proton hole in  $f_{7/2}$  and at least one neutron in shape driving  $g_{9/2}$  orbitals for the lower spin with the most probable configuration of  $\pi(f_{7/2}^{-1}(p_{3/2})^1) \otimes \nu(g_{9/2}^1(fp)^4)$ . As the band proceed to the higher spin it is clearly seen in Fig. 17(b), that the occupation of proton in  $0f_{7/2}$  reduces after  $21/2^+$  whereas the occupation in  $0f_{5/2}$  increases. Therefore, an extra proton is predicted to be promoted in the  $fp$  shell from  $0f_{7/2}$  after  $21/2^+$  and the configuration of the higher spin states for Band B4 is emerged as  $\pi(f_{7/2}^{-2}p_{3/2}^1f_{5/2}) \otimes \nu(g_{9/2}^1(fp)^4)$ . This SM predicted configuration is well matched with the structure of band B4 discussed above. For Band B2 the SM predicted level energies for each spins are over-estimated than the experimental states and thus are not shown along with experimental data in Fig.13. However from the SM calculated occupation number of proton and neutron for Band B2 in Fig. 17(a) and (b), it may be predicted that this band also contains at least one proton hole in  $0f_{7/2}$  and one neutron in  $0g_{9/2}$ . The  $B(E2)$  values for this band is found out to be around  $120 \text{ e}^2 \text{ fm}^2$  on average from SM. As discussed above, from the comparison with the neighboring nuclei in Fig. 16, the aligned angular momentum  $I_x$  of this band is little bit higher and matched with the bands having configuration involving  $\nu g_{9/2}^2$ . It is beyond the scope of the present SM

calculation to have more than one particle to cross the  $fp$  shell and occupy the  $g_{9/2}$  or  $d_{5/2}$  orbitals. That may be the reason behind the fact that the experimental excited states of Band B2 do not match well with the SM calculated states.

## VI. SUMMARY

In the present work we have studied the structure of  $^{61}\text{Ni}$  using the  $^{14}\text{C}$  beam from the John D Fox laboratory at FSU incident on a thin  $^{50}\text{Ti}$  target and using the FSU gamma array to detect the  $\gamma$  rays. The spectroscopic information on  $^{61}\text{Ni}$  has been extended considerably up to  $\approx 13$  MeV and  $35/2^+$  spin/parity with the establishment of 28 new levels and 76 new transitions decaying from those levels. The spin and parity of most of the states have been assigned from DCO ratios and  $\Delta_{IPDCO}$  measurements of the  $\gamma$  rays. With  $Z=28$  for  $^{61}\text{Ni}$ , the low lying negative-parity states are found to be generated from single particle excitations of the odd neutrons in the  $\nu p_{3/2}$ ,  $\nu f_{5/2}$  and  $\nu p_{1/2}$  orbitals as expected. For the positive parity states, one neutron must be promoted to the next shell  $0g_{9/2}$  or  $2d_{5/2}$  orbitals. The shell model calculation using the GXPf1Br+ $V_{MU}$ (modified) interaction within a model space of  $fp$ -shell +  $\nu g_{9/2}$  +  $\nu d_{5/2}$  reproduced the negative as well as positive parity states pretty well. Apart from the low lying irregular structure, two magnetic rotational (MR) bands Band B1 and Band B3 with a regular sequence of M1 transitions have been established. The shears mechanism associated with the MR band are described by the semi classical model. With a single value of  $j_\pi$  and  $j_\nu$ , the SCM cannot fit the Band B1 entirely. Therefore the values of  $j_\pi$  and  $j_\nu$  are chosen wisely to have the shears mechanism starts at  $21/2^+$  (upper part of Band B1) with the shears angle  $\approx 90^\circ$  and continued up to maximum observed spin at  $29/2^+$  by closing the shears angle between the proton and the neutron arms. With this consideration, and SCM fit matched pretty well with the experimental data. The experimental levels corresponding to Band B3 are found to be associated with same  $j_\pi$  and  $j_\nu$  values from SCM fit to form the shears. The shell model calculations predict the configuration for these bands involving one high-j  $\pi f_{7/2}$  holes and one high-j  $\nu g_{9/2}$  particle. The shell model predicted a high  $B(M1)$  values for these two bands which further indicate them to be of magnetic rotational type.

The average halflives of the Band B1 and Band B3 are calculated to be of the order of 0.1 ps and 0.7 ps, respectively from the shell model  $B(M1)$  values which are in line with what is expected for magnetic rotational bands. With the involvement of the shape driving  $\nu g_{9/2}$  orbital, a small deformation is expected to be induced into the system. The formation of two deformed collective bands named Bands B2 and B4 with regular E2 transitions established the onset of deformation in this nuclei at higher energy. The excited energies of the collective bands are plotted as a function of spin for better understanding. The Band B4 are extended beyond the band crossing and an extra proton is predicted to be excited from the lower shell to upper  $fp$  shell around  $21/2^+$ . The SM predicts the energy levels of the Band B1 and B4 matched quite well with the experimental data within the considered model space whereas it overestimated the energies for Band B2 and Band B3. The occupation number of different orbitals for proton and neutrons, corresponding to different bands are plotted as a function of spin for these collective structures which indicate the configurations associated with them. The Band B2 is seen not to be well developed from the present data and future experimental effort to extend this band would reveal additional information. Along with the extension of the quadrupole bands, the lifetime measurements of the levels of the magnetic rotational bands (B1 and B3) will be interesting to understand these structures better and will be our next experimental goal.

## VII. ACKNOWLEDGEMENT

This work was supported by the U.S. National Science Foundation under Grant Nos. PHY-2012522 (FSU) and U.S. Department of Energy, office of Science under Awards No. DE-AC05-00OR22725 (ORNL). Y. Utsumo and N. Shimizu acknowledge KAKENHI grants (20K03981, 17K05433), "Priority Issue on post-K computer" (hp190160, hp180179, hp170230) and "Program for Promoting Researches on the Supercomputer Fugaku" (hp200130, hp210165). The authors are thankful to Mr. Shabir Dar, VECC, Kolkata, India for providing his semi-classical geometrical model code to fit the magnetic rotational band. We acknowledge the useful discussion with Dr. S. Bhattacharyya, VECC, Kolkata, India.

---

[1] A. Gade, R. V. F. Janssens, D. Bazin, R. Broda, B. A. Brown, C. M. Campbell, M. P. Carpenter, J. M. Cook, A. N. Deacon, D.-C. Dinca, B. Fornal, S. J. Freeman, T. Glasmacher, P. G. Hansen, B. P. Kay, P. F. Mantica, W. F. Mueller, J. R. Terry, J. A. Tostevin, and S. Zhu, Cross-shell excitation in two-proton knockout: Structure of  $^{52}\text{Ca}$ , Phys. Rev. C **74**, 021302(R) (2006).

[2] R. V. F. Janssens, B. Fornal, P. F. Mantica, B. A. Brown, R. Broda, P. Bhattacharyya, M. P. Carpenter, M. Cinausero, P. J. Daly, A. D. Davies, T. Glasmacher, Z. W. Grabowski, D. E. Groh, M. Honma, F. G. Kondev, W. Królás, T. Lauritsen, S. N. Liddick, S. Lunardi, N. Marginean, T. Mizusaki, D. J. Morrissey, A. C. Morton, W. F. Mueller, T. Otsuka, T. Pawlat, D. Seweryniak, H. Schatz, A. Stolz, S. L. Tabor, C. A. Ur, G. Vi-

- esti, I. Wiedenhöver, and J. Wrzesiński, Structure of  $^{52,54}\text{Ti}$  and shell closures in neutron-rich nuclei above  $^{48}\text{Ca}$ , *Physics Letters B* **546**, 55 (2002).
- [3] J. I. Prisciandaro, P. F. Mantica, B. A. Brown, D. W. Anthony, M. W. Cooper, A. Garcia, D. E. Groh, A. Komives, W. Kumarasiri, P. A. Lofy, A. M. Oros-Peusquens, S. L. Tabor, and M. Wiedeking, New evidence for a subshell gap at  $N=32$ , *Physics Letters B* **510**, 17 (2001).
- [4] A. Gade, R. V. F. Janssens, T. Baugher, D. Bazin, B. A. Brown, M. P. Carpenter, C. J. Chiara, A. N. Deacon, S. J. Freeman, G. F. Grinyer, C. R. Hoffman, B. P. Kay, F. G. Kondev, T. Lauritsen, S. McDaniel, K. Meierbachtol, A. Ratkiewicz, S. R. Stroberg, K. A. Walsh, D. Weisshaar, R. Winkler, and S. Zhu, Collectivity at  $N = 40$  in neutron-rich  $^{64}\text{Cr}$ , *Phys. Rev. C* **81**, 051304(R) (2010).
- [5] P. Adrich, A. M. Amthor, D. Bazin, M. D. Bowen, B. A. Brown, C. M. Campbell, J. M. Cook, A. Gade, D. Galaviz, T. Glasmacher, S. McDaniel, D. Miller, A. Obertelli, Y. Shimbara, K. P. Siwek, J. A. Tostevin, and D. Weisshaar, In-beam  $\gamma$ -ray spectroscopy and inclusive two-proton knockout cross section measurements at  $N \approx 40$ , *Phys. Rev. C* **77**, 054306 (2008).
- [6] R. Broda, T. Pawlat, W. Królas, R. V. F. Janssens, S. Zhu, W. B. Walters, B. Fornal, C. J. Chiara, M. P. Carpenter, N. Hoteling, L. W. Iskra, F. G. Kondev, T. Lauritsen, D. Seweryniak, I. Stefanescu, X. Wang, and J. Wrzesiński, Spectroscopic study of the  $^{64,66,68}\text{Ni}$  isotopes populated in  $^{64}\text{Ni} + ^{238}\text{U}$  collisions, *Phys. Rev. C* **86**, 064312 (2012).
- [7] J. P. Schiffer, C. R. Hoffman, B. P. Kay, J. A. Clark, C. M. Deibel, S. J. Freeman, M. Honma, A. M. Howard, A. J. Mitchell, T. Otsuka, P. D. Parker, D. K. Sharp, and J. S. Thomas, Valence nucleon populations in the Ni isotopes, *Phys. Rev. C* **87**, 034306 (2013).
- [8] M. Bernas, P. Dessagne, M. Langevin, J. Payet, F. Pougheon, and P. Roussel, Magic features of  $^{68}\text{Ni}$ , *Physics Letters B* **113**, 279 (1982).
- [9] S. Zhu, R. V. F. Janssens, M. P. Carpenter, C. J. Chiara, R. Broda, B. Fornal, N. Hoteling, W. Królas, T. Lauritsen, T. Pawlat, D. Seweryniak, I. Stefanescu, J. R. Stone, W. B. Walters, X. Wang, and J. Wrzesiński, Nature of yrast excitations near  $N = 40$ : Level structure of  $^{67}\text{Ni}$ , *Phys. Rev. C* **85**, 034336 (2012).
- [10] E. K. Johansson, D. Rudolph, L.-L. Andersson, D. A. Torres, I. Ragnarsson, C. Andreoiu, C. Baktash, M. P. Carpenter, R. J. Charity, C. J. Chiara, J. Ekman, C. Fahlander, C. Hoel, O. L. Pechenaya, W. Reviol, R. du Rietz, D. G. Sarantites, D. Seweryniak, L. G. Sobotka, C. H. Yu, and S. Zhu, Prompt proton decay and deformed bands in  $^{56}\text{Ni}$ , *Phys. Rev. C* **77**, 064316 (2008).
- [11] D. Rudolph, I. Ragnarsson, W. Reviol, C. Andreoiu, M. A. Bentley, M. P. Carpenter, R. J. Charity, R. M. Clark, M. Cromaz, J. Ekman, C. Fahlander, P. Fallon, E. Ideguchi, A. O. Macchiavelli, M. N. Mineva, D. G. Sarantites, D. Seweryniak, and S. J. Williams, Rotational bands in the semi-magic nucleus  $^{57}_{28}\text{Ni}_{29}$ , *Journal of Physics G: Nuclear and Particle Physics* **37**, 075105 (2010).
- [12] E. K. Johansson, D. Rudolph, I. Ragnarsson, L. L. Andersson, D. A. Torres, C. Andreoiu, C. Baktash, M. P. Carpenter, R. J. Charity, C. J. Chiara, J. Ekman, C. Fahlander, O. L. Pechenaya, W. Reviol, R. du Rietz, D. G. Sarantites, D. Seweryniak, L. G. Sobotka, C. H. Yu, and S. Zhu, Thorough  $\gamma$ -ray and particle decay investigations of  $^{58}\text{Ni}$ , *Phys. Rev. C* **80**, 014321 (2009).
- [13] C.-H. Yu, C. Baktash, J. A. Cameron, M. Devlin, J. Eberth, A. Galindo-Uribarri, D. S. Haslip, D. R. LaFosse, T. J. Lampman, I.-Y. Lee, F. Lerma, A. O. Macchiavelli, S. D. Paul, D. C. Radford, I. Ragnarsson, D. Rudolph, D. G. Sarantites, C. E. Svensson, J. C. Waddington, J. C. Wells, and J. N. Wilson, Rotational bands with terminating properties in  $^{59}\text{Ni}$ , *Phys. Rev. C* **65**, 061302(R) (2002).
- [14] D. A. Torres, F. Cristancho, L.-L. Andersson, E. K. Johansson, D. Rudolph, C. Fahlander, J. Ekman, R. du Rietz, C. Andreoiu, M. P. Carpenter, D. Seweryniak, S. Zhu, R. J. Charity, C. J. Chiara, C. Hoel, O. L. Pechenaya, W. Reviol, D. G. Sarantites, L. G. Sobotka, C. Baktash, C.-H. Yu, B. G. Carlsson, and I. Ragnarsson, Deformations and magnetic rotations in the  $^{60}\text{Ni}$  nucleus, *Phys. Rev. C* **78**, 054318 (2008).
- [15] M. Albers, S. Zhu, R. V. F. Janssens, J. Gellanki, I. Ragnarsson, M. Alcorta, T. Baugher, P. F. Bertone, M. P. Carpenter, C. J. Chiara, P. Chowdhury, A. N. Deacon, A. Gade, B. DiGiovine, C. R. Hoffman, F. G. Kondev, T. Lauritsen, C. J. Lister, E. A. McCutchan, D. S. Moerland, C. Nair, A. M. Rogers, and D. Seweryniak, Single-particle and collective excitations in  $^{63}\text{Ni}$ , *Phys. Rev. C* **88**, 054314 (2013).
- [16] S. Samanta, S. Das, R. Bhattacharjee, S. Chatterjee, R. Raut, S. S. Ghugre, A. K. Sinha, U. Garg, Nee-lam, N. Kumar, P. Jones, M. S. R. Laskar, F. S. Babra, S. Biswas, S. Saha, P. Singh, and R. Palit, Single particle configurations in  $^{61}\text{Ni}$ , *Phys. Rev. C* **99**, 014315 (2019).
- [17] P. W. Zhao, S. Q. Zhang, J. Peng, H. Z. Liang, P. Ring, and J. Meng, Novel structure for magnetic rotation bands in  $^{60}\text{Ni}$ , *Physics Letters B* **699**, 181 (2011).
- [18] S. Ganguly, C. Majumder, S. S. Tiwary, H. P. Sharma, and S. Chakraborty, Magnetic rotation in  $^{60}\text{Ni}$ : A semiclassical description., *Acta Physica Polonica B* **51**, 473 (2020).
- [19] N. Sensharma, A. D. Ayangeakaa, R. V. F. Janssens, Q. B. Chen, S. Zhu, M. Alcorta, M. P. Carpenter, E. A. McCutchan, F. G. Kondev, T. Lauritsen, D. Seweryniak, C. R. Hoffman, A. M. Rogers, A. Gade, T. Baugher, and P. Chowdhury, Single-particle and dipole excitations in  $^{62}\text{Co}$ , *Phys. Rev. C* **105**, 044315 (2022).
- [20] L. Hu, J. Peng, and Q. B. Chen, Possible existence of multiple wobbling modes in  $A \approx 60$  nuclei, *Phys. Rev. C* **104**, 064325 (2021).
- [21] R. Wadsworth, A. Kogan, P. R. G. Lornie, M. R. Nixon, H. G. Price, and P. J. Twin, Gamma ray spectroscopy in  $^{61}\text{Ni}$ -levels below 2.2 MeV in excitation, *Journal of Physics G: Nuclear Physics* **3**, 35 (1977).
- [22] R. Wadsworth, G. D. Jones, A. Kogan, P. R. G. Lornie, T. Morrison, O. Mustafa, H. G. Price, D. Simister, and P. J. Twin, Gamma ray spectroscopy in  $^{61}\text{Ni}$ -levels above 2.2 MeV in excitation, *Journal of Physics G: Nuclear Physics* **3**, 833 (1977).
- [23] E. K. Warburton, J. W. Olness, A. M. Nathan, and A. R. Poletti, Yrast decay schemes from heavy-ion +  $^{48}\text{Ca}$  fusion-evaporation reactions: Iv:  $^{53}\text{Cr}$ ,  $^{54}\text{V}$ ,  $^{62}\text{Co}$ , and  $^{61-63}\text{Ni}$ , *Phys. Rev. C* **18**, 1637 (1978).
- [24] E. Rubino, S. L. Tabor, V. Tripathi, R. S. Lubna, B. Abromeit, J. M. Allmond, L. T. Baby, D. D. Caussyn, K. Kravvaris, and A. Volya, Multiparticle-hole excita-

- tions in nuclei near  $N = Z = 20$ :  $^{41}\text{K}$ , Eur. Phys. J. A **58**, 10.1140/epja/s10050-022-00755-1 (2022).
- [25] R. S. Lubna, K. Kravvaris, S. L. Tabor, V. Tripathi, A. Volya, E. Rubino, J. M. Allmond, B. Abromeit, L. T. Baby, and T. C. Hensley, Structure of  $^{38}\text{Cl}$  and the quest for a comprehensive shell model interaction, Phys. Rev. C **100**, 034308 (2019).
- [26] J. Pavan, Thesis, Ph.D., Florida State University, Tallahassee, Florida, 2003 (unpublished). (1998).
- [27] FSU, Website, [http://fsunuc.physics.fsu.edu/caussyn/]. (2013).
- [28] D. Radford, Escl8r and levit8r: Software for interactive graphical analysis of hpge coincidence data sets, Nuclear Instruments and Methods in Physics Research Section A: Accelerators, Spectrometers, Detectors and Associated Equipment **361**, 297 (1995).
- [29] A. Krämer-Flecken, T. Morek, R. M. Lieder, W. Gast, G. Hebbinghaus, H. M. Jäger, and W. Urban, Use of dco ratios for spin determination in  $\gamma - \gamma$  coincidence measurements, Nuclear Instruments and Methods in Physics Research Section A: Accelerators, Spectrometers, Detectors and Associated Equipment **275**, 333 (1989).
- [30] K. Starosta, T. Morek, C. Droste, S. G. Rohoziński, J. Srebrny, A. Wierzchucka, M. Bergström, B. Herskind, E. Melby, T. Czosnyka, and P. J. Napiorkowski, Experimental test of the polarization direction correlation method (pdco), Nuclear Instruments and Methods in Physics Research Section A: Accelerators, Spectrometers, Detectors and Associated Equipment **423**, 16 (1999).
- [31] C. Droste, S. G. Rohoziński, K. Starosta, T. Morek, J. Srebrny, and P. Magierski, Pdco: Polarizational-directional correlation from oriented nuclei, Nuclear Instruments and Methods in Physics Research Section A: Accelerators, Spectrometers, Detectors and Associated Equipment **378**, 518 (1996).
- [32] S. Bhattacharya, S. Bhattacharyya, R. Banik, S. Das Gupta, G. Mukherjee, A. Dhal, S. S. Alam, M. A. Asgar, T. Roy, A. Saha, S. Nandi, T. Bhattacharjee, A. Choudhury, D. Mondal, S. Mukhopadhyay, P. Mukhopadhyay, S. Pal, D. Pandit, I. Shaik, and S. R. Banerjee, Yrast and non-yrast spectroscopy of  $^{199}\text{Tl}$  using  $\alpha$ -induced reactions, Phys. Rev. C **98**, 044311 (2018).
- [33] T. Togashi, N. Shimizu, Y. Utsuno, T. Otsuka, and M. Honma, Large-scale shell-model calculations for unnatural-parity high-spin states in neutron-rich Cr and Fe isotopes, Phys. Rev. C **91**, 024320 (2015).
- [34] S. Frauendorf, Tilted cranking, Nuclear Physics A **557**, 259c (1993).
- [35] R. M. Clark and A. O. Macchiavelli, The shears mechanism in nuclei, Annual Review of Nuclear and Particle Science **50**, 1 (2000).
- [36] A. O. Macchiavelli, R. M. Clark, P. Fallon, M. A. Deleplanque, R. M. Diamond, R. Krücken, I. Y. Lee, F. S. Stephens, S. Asztalos, and K. Vetter, Semiclassical description of the shears mechanism and the role of effective interactions, Phys. Rev. C **57**, R1073 (1998).
- [37] A. O. Macchiavelli, R. M. Clark, M. A. Deleplanque, R. M. Diamond, P. Fallon, I. Y. Lee, F. S. Stephens, and K. Vetter, Rotational-like properties of the shears bands, Phys. Rev. C **58**, 3746 (1998).
- [38] G. Baldsiefen, H. Hubel, W. Korten, D. Mehta, N. Nenoff, B. V. Rao, P. Willsau, H. Grawe, J. Heese, H. Kluge, K. H. Maier, R. Schubart, S. Frauendorf, and H. J. Maier, “shears bands” in  $^{199}\text{Pb}$  and  $^{200}\text{Pb}$ , Nuclear Physics A **574**, 521 (1994).
- [39] S. Frauendorf, Spontaneous symmetry breaking in rotating nuclei, Rev. Mod. Phys. **73**, 463 (2001).
- [40] A. N. Deacon, S. J. Freeman, R. V. F. Janssens, M. Honma, M. P. Carpenter, P. Chowdhury, T. Lauritsen, C. J. Lister, D. Seweryniak, J. F. Smith, S. L. Tabor, B. J. Varley, F. R. Xu, and S. Zhu, Yrast structures in the neutron-rich isotopes  $^{59,60}\text{Fe}$  and the role of the  $g_{9/2}$  orbital, Phys. Rev. C **76**, 054303 (2007).

## VIII. APPENDIX

TABLE I: The energies of the  $\gamma$ -ray transitions ( $E_\gamma$ ), energies of the initial levels ( $E_i$ ), the spins and parities of the initial ( $J_i^\pi$ ) and final ( $J_f^\pi$ ) levels along with the relative intensities ( $I_\gamma$ ), DCO ratios ( $R_{DCO}$ ) and IPDCO values ( $\Delta_{IPDCO}$ ) and the proposed multipolarities for all observed transitions in  $^{61}\text{Ni}$  from the present work are listed. The  $\gamma$  ray energies are determined from spectra displayed with 1.0 keV/Ch dispersion. The errors listed adjacent to each  $\gamma$  transition represent the fitting error. The observed  $\gamma$ -ray intensities are estimated from prompt spectra and normalized to 100 for the intensity of 67-keV  $\gamma$ -ray. The spin and parity of the states which cannot be determined from the present data are either presented in parentheses or adopted from the earlier work. The multipolarity and nature of few transitions, for which  $R_{DCO}$  or  $\Delta_{IPDCO}$  could not be determined or ambiguous, are presented in parenthesis or fixed from the initial and final level spin-parity value.

\*The intensity is less than 0.2% of the intensity of 67 keV.

#The intensity could not be determined from present data due to overlap with nearby energies.

§ DCO ratio in E2 gating transition.

& DCO ratio in E1 gating transition.

$E_\gamma$ (in keV)	$J_i^\pi \rightarrow J_f^\pi$	$E_i$ (in keV)	$E_f$ (in keV)	$I_\gamma(\text{Err})$	$R_{DCO}$ (Err)	$\Delta_{IPDCO}$	Deduced Multipolarity
67.2(1)	$5/2^- \rightarrow 3/2^-$	67.2(1)	0.0(-)	100(3)	0.63(5) <sup>§</sup>	-	M1

Table I: Continued...

$E_\gamma$ (in keV)	$J_i^\pi \rightarrow J_f^\pi$	$E_i$ (in keV)	$E_f$ (in keV)	$I_\gamma$ (Err)	$R_{DCO}$ (Err)	$\Delta IPDCO$	Deduced Multipolarity
134.2(1)	$9/2^+ \rightarrow 9/2^-$	2121.0(1)	1987.0(1)	0.32(4)	-	-	E1
136.6(1)	$13/2^+ \rightarrow 11/2^+$	3434.9(2)	3298.4(5)	7.52(23)	-	-	M1
207.0(1)	$15/2^+ \rightarrow 13/2^{(+)}$	5147.3(3)	4939.8(2)	0.97(4)	-	-	(M1)
320.2(2)	$17/2^+ \rightarrow 17/2^+$	5630.9(3)	5310.7(2)	0.77(3)	-	-	M1
321.0(3)	$11/2^- \rightarrow 9/2^-$	2128.3(1)	1807.4(1)	$< 0.2^*$	-	-	M1
348.8(1)	$23/2^+ \rightarrow 21/2^+$	8027.7(2)	7678.9(2)	2.14(6)	0.61(4) <sup>§</sup>	-0.19(6)	M1
384.2(2)	$15/2^+ \rightarrow 13/2^+$	5147.3(3)	4762.9(2)	1.73(6)	-	-	M1
422.7(3)	$23/2^+ \rightarrow 23/2^+$	8027.7(2)	2128.3(1)	1.71(4)	0.78(5) <sup>§</sup>	-0.06(2)	M1+E2
483.7(1)	$17/2^+ \rightarrow 15/2^+$	5630.9(3)	5147.3(3)	8.29(17)	0.58(3) <sup>§</sup>	-0.11(2)	M1
492.4(1)	$17/2^+ \rightarrow 17/2^+$	5310.7(2)	4818.3(2)	6.9(8)	-	-	M1
525.0(2)	$25/2^+ \rightarrow 23/2^+$	8552.7(3)	8027.7(2)	2.99(14)	0.67(4) <sup>§</sup>	-0.06(2)	M1
532.8(2)	$9/2^- \rightarrow 7/2^-$	1987.0(1)	1454.4(1)	1.06(2)	0.70(4) <sup>§</sup>	-0.07(2)	M1+E2
552.6(1)	$23/2^+ \rightarrow 21/2^+$	7790.6(3)	7237.9(3)	0.88(3)	1.00(5) <sup>§&amp;</sup>	-0.25(15)	M1
562.0(1)	$19/2^+ \rightarrow 17/2^+$	6192.9(2)	5630.9(3)	7.73(16)	0.66(3) <sup>§</sup>	-0.06(2)	M1
583.8(1)	$15/2^+ \rightarrow 13/2^+$	4018.7(2)	3434.9(2)	6.30(13)	0.95(5) <sup>§</sup>	-0.20(5)	M1+E2
592.8(1)	$15/2^+ \rightarrow 13/2^-$	4018.7(2)	3426.0(2)	10.56(25)	0.50(2) <sup>§</sup>	0.02(1)	E1
625.2(2)	$15/2^+ \rightarrow 15/2^{(+)}$	5147.3(3)	4522.0(5)	0.72(3)	0.90(7) <sup>§&amp;</sup>	-	(M1+E2)
666.8(3)	$9/2^+ \rightarrow 7/2^-$	2121.0(1)	1454.4(1)	0.34(2)	0.59(7) <sup>§</sup>	-	E1
669.2(3)	$21/2^+ \rightarrow 19/2^+$	6734.3(2)	6065.1(2)	$< 0.2^*$	-	-	M1
670.4(3)	$15/2^+ \rightarrow 15/2^+$	5147.3(3)	4476.9(2)	1.85(5)	0.94(7) <sup>§</sup>	-	M1+E2
678.8(2)	$17/2^+ \rightarrow 15/2^+$	5155.7(2)	4476.9(2)	1.83(5)	1.10(6) <sup>§&amp;</sup>	-	M1+E2
720.6(2)	$15/2^+ \rightarrow 11/2^+$	4018.7(2)	3298.4(5)	4.23(9)	1.54(8) <sup>§&amp;</sup>	0.12(4)	E2
754.4(1)	$19/2^+ \rightarrow 17/2^+$	6065.1(2)	5310.7(2)	1.28(4)	1.20(6) <sup>§&amp;</sup>	-0.07(3)	M1+E2
769.2(6)	$17/2^+ \rightarrow 17/2^+$	5925.2(2)	5155.7(2)	0.90(3)	0.85(6) <sup>§</sup>	-	M1+E2
778.8(2)	$21/2^+ \rightarrow 19/2^+$	6971.6(3)	6192.9(2)	7.31(19)	0.75(4) <sup>§</sup>	-0.07(1)	M1+E2
783.9(2)	$27/2^+ \rightarrow 25/2^+$	9336.6(4)	8552.7(3)	2.67(18)	0.73(4) <sup>§</sup>	-	M1+E2
792.4(1)	$9/2^- \rightarrow 7/2^-$	1807.4(1)	1014.9(1)	2.18(6)	-	-	M1
799.4(1)	$17/2^+ \rightarrow 15/2^+$	4818.3(2)	4018.7(2)	8.63(18)	0.51(3) <sup>§</sup>	-0.03(1)	M1
812.6(2)	$17/2^+ \rightarrow 17/2^+$	5630.9(3)	4818.3(2)	6.9(7)	-	-	M1
819.0(1)	$23/2^+ \rightarrow 21/2^+$	7790.6(3)	6971.6(3)	2.93(7)	0.75(4) <sup>§</sup>	-0.12(3)	M1+E2
833.8(1)	$17/2^+ \rightarrow 15/2^+$	5310.7(2)	4476.9(2)	4.31(14)	0.74(4) <sup>§</sup>	-	M1+E2
840.6(1)	$5/2^- \rightarrow 5/2^-$	907.6(1)	67.2(1)	3.54(32)	-	-	M1
863.4(2)	$29/2^+ \rightarrow 27/2^+$	10200.0(4)	9336.6(4)	1.12(8)	0.54(3) <sup>§</sup>	-	M1
872.4(2)	$25/2^+ \rightarrow 23/2^+$	8663.0(3)	7790.6(3)	3.59(9)	1.07(6) <sup>§&amp;</sup>	-0.09(2)	M1
882.2(1)	$19/2^+ \rightarrow 17/2^+$	6192.9(2)	5310.7(2)	6.12(13)	0.99(5) <sup>§&amp;</sup>	-0.07(1)	M1
907.6(3)	$13/2^+ \rightarrow 11/2^+$	4206.3(2)	3298.4(5)	3.02(10)	1.14(8) <sup>§&amp;</sup>	-	M1+E2
907.7(1)	$5/2^- \rightarrow 3/2^-$	907.6(1)	0.0(-)	6.9(7)	0.58(4) <sup>§</sup>	-	M1
909.4(1)	$19/2^+ \rightarrow 17/2^+$	6065.1(2)	5155.7(2)	0.69(8)	0.73(7) <sup>§</sup>	-	M1+E2
924.7(3)	$19/2^+ \rightarrow 17/2^+$	6555.7(3)	5630.9(3)	1.75(7)	0.74(4) <sup>§</sup>	-0.05(1)	M1+E2
938.4(5)	$(31/2^+) \rightarrow 29/2^+$	11138.4(7)	10200.0(4)	$< 0.2^*$	-	-	M1
941.0(1)	$15/2^+ \rightarrow 13/2^+$	5147.3(3)	4206.3(2)	5.20(12)	0.65(7) <sup>§</sup>	-0.01(1)	M1
947.7(1)	$7/2^- \rightarrow 5/2^-$	1014.9(1)	67.2(1)	68.5(14)	1.38(4) <sup>§&amp;</sup>	-0.04(1)	M1+E2
955.2(2)	$9/2^- \rightarrow 7/2^-$	2409.4(1)	1454.4(1)	0.21(1)	-	-	M1
967.4(7)	$15/2^{(-)} \rightarrow 13/2^+$	4999.3(2)	4032.1(2)	$< 0.2^*$	-	-	E1
972.2(1)	$9/2^- \rightarrow 7/2^-$	1987.0(1)	1014.9(1)	5.67(12)	0.43(2) <sup>§</sup>	-0.02(1)	M1+E2
1014.9(1)	$7/2^- \rightarrow 3/2^-$	1014.9(1)	0.0(-)	31.8(6)	0.83(3) <sup>§</sup>	0.07(1)	E2
1042.0(1)	$15/2^+ \rightarrow 13/2^+$	4476.9(2)	3434.9(2)	13.2(3)	0.78(2) <sup>§</sup>	-0.07(1)	M1+E2
1045.4(3)	$21/2^+ \rightarrow 19/2^+$	7237.9(3)	6192.9(2)	$< 0.2^*$	-	-	M1
1079.2(2)	$9/2^- \rightarrow 5/2^-$	1987.0(1)	907.6(1)	10.51(19)	1.01(3) <sup>§</sup>	-0.02(2)	E2
1084.6(2)	$27/2^+ \rightarrow 25/2^+$	9747.6(4)	8663.0(3)	1.59(6)	-	-	M1
1106.1(1)	$9/2^+ \rightarrow 7/2^-$	2121.0(1)	1014.9(1)	68.4(2)	0.62(2) <sup>§</sup>	0.04(1)	E1
1113.4(1)	$11/2^- \rightarrow 7/2^-$	2128.3(1)	1014.9(1)	35.7(7)	0.95(3) <sup>§</sup>	0.04(1)	E2
1128.2(5)	$15/2^+ \rightarrow 15/2^+$	5147.3(3)	4018.7(2)	1.26(5)	1.04(6) <sup>§&amp;</sup>	-	M1
1132.3(5)	$5/2^- \rightarrow 3/2^-$	1132.3(5)	0.0(-)	$< 0.2^*$	-	-	M1
1136.8(1)	$17/2^+ \rightarrow 15/2^+$	5155.7(2)	4018.7(2)	1.42(5)	0.88(5) <sup>§&amp;</sup>	-	M1+E2
1177.4(5)	$11/2^+ \rightarrow 9/2^+$	3298.4(5)	2121.0(1)	17.6(6)	1.24(9) <sup>§&amp;</sup>	-0.03(1)	M1+E2
1178.6(5)	$15/2^+ \rightarrow 11/2^+$	4476.9(2)	3298.4(5)	5.3(9)	-	-	E2

Table I: Continued...

$E_\gamma$ (in keV)	$J_i^\pi \rightarrow J_f^\pi$	$E_i$ (in keV)	$E_f$ (in keV)	$I_\gamma$ (Err)	$R_{DCO}$ (Err)	$\Delta_{IPDCO}$	Deduced Multipolarity
1223.6(2)	$15/2^{(+)} \rightarrow 11/2^{+}$	4522.0(5)	3298.4(5)	1.59(5)	1.78(10) <sup>&amp;</sup>	-	(E2)
1246.8(2)	$19/2^{+} \rightarrow 17/2^{+}$	6065.1(2)	4818.3(2)	1.08(2)	0.96(5) <sup>&amp;</sup>	-0.19(8)	M1
1271.2(1)	$13/2^{(-)} \rightarrow 9/2^{-}$	3258.2(2)	1987.0(1)	0.57(1)	0.95(6) <sup>§</sup>	-	(E2)
1277.2(6)	$9/2^{-} \rightarrow 5/2^{-}$	2409.4(1)	1132.3(5)	$< 0.2^*$	-	-	E2
1291.8(3)	$17/2^{+} \rightarrow 15/2^{+}$	5310.7(2)	4018.7(2)	4.31(12)	1.12(6) <sup>&amp;</sup>	-0.05(1)	M1+E2
1295.4(4)	$(29/2^{+}) \rightarrow 27/2^{+}$	11043.0(6)	9747.6(4)	$< 0.2^*$	-	-	(M1)
1297.9(3)	$13/2^{-} \rightarrow 11/2^{-}$	3426.0(2)	2128.3(1)	9.38(17)	0.59(4) <sup>§</sup>	-	M1
1306.8(3)	$13/2^{+} \rightarrow 11/2^{-}$	3434.9(2)	2128.3(1)	1.69(7)	0.44(2) <sup>§</sup>	-	E1
1313.9(1)	$13/2^{+} \rightarrow 9/2^{+}$	3434.9(2)	2121.0(1)	37.3(7)	0.99(3) <sup>§</sup>	0.05(1)	E2
1339.7(2)	$15/2^{(-)} \rightarrow 13/2^{-}$	4766.0(3)	3426.0(2)	1.17(7)	0.54(4) <sup>§</sup>	-	(M1)
1341.0(5)	$21/2^{+} \rightarrow 17/2^{+}$	6971.6(3)	5630.9(3)	$< 0.2^*$	-	-	E2
1341.8(3)	$21/2^{+} \rightarrow 17/2^{+}$	7266.9(2)	5925.2(2)	1.76(4)	1.04(6) <sup>§</sup>	0.03(1)	E2
1374.6(2)	$19/2^{+} \rightarrow 17/2^{+}$	6192.9(2)	4818.3(2)	0.34(3)	-	-	M1
1383.4(1)	$17/2^{+} \rightarrow 13/2^{+}$	4818.3(2)	3434.9(2)	6.9(7)	0.93(5) <sup>§</sup>	-	E2
1387.2(5)	$7/2^{-} \rightarrow 5/2^{-}$	1454.4(1)	67.2(1)	$< 0.2^*$	0.66(5) <sup>§</sup>	-	M1
1394.2(2)	$9/2^{-} \rightarrow 7/2^{-}$	2409.4(1)	1014.9(1)	1.30(3)	-	-	M1
1412.0(2)	$23/2^{+} \rightarrow 19/2^{+}$	7604.9(3)	6192.9(2)	0.65(2)	-	-	E2
1438.7(2)	$13/2^{-} \rightarrow 9/2^{-}$	3426.0(2)	1987.0(1)	3.75(8)	1.01(5) <sup>§</sup>	0.06(1)	E2
1450.9(1)	$13/2^{(-)} \rightarrow 9/2^{-}$	3258.2(2)	1807.4(1)	0.17(1)	-	-	(E2)
1454.4(1)	$7/2^{-} \rightarrow 3/2^{-}$	1454.4(1)	0.0(-)	14.9(3)	0.96(3) <sup>§</sup>	0.10(6)	E2
1501.9(3)	$27/2^{+} \rightarrow 23/2^{+}$	9106.8(4)	7604.9(3)	2.40(2)	1.57(8) <sup>&amp;</sup>	0.02(2)	E2
1505.1(3)	$13/2^{(+)} \rightarrow 13/2^{+}$	4939.8(2)	3434.9(2)	3.90(8)	0.96(5) <sup>§</sup>	0.01(2)	(M1+E2)
1507.7(3)	$15/2^{(-)} \rightarrow 13/2^{(-)}$	4766.0(3)	3258.2(2)	$< 0.2^*$	-	-	(M1)
1539.8(1)	$23/2^{+} \rightarrow 19/2^{+}$	7604.9(3)	6065.1(2)	4.78(8)	0.96(6) <sup>§</sup>	0.02(1)	E2
1578.6(1)	$21/2^{+} \rightarrow 17/2^{+}$	6734.3(2)	5155.7(2)	5.36(11)	0.95(5) <sup>§</sup>	0.06(3)	E2
1588.2(2)	$19/2^{+} \rightarrow 15/2^{+}$	6065.1(2)	4476.9(2)	4.39(10)	1.05(6) <sup>§</sup>	0.09(6)	E2
1607.0(3)	$21/2^{+} \rightarrow 17/2^{+}$	7237.9(3)	5630.9(3)	$< 0.2^*$	-	-	E2
1611.8(1)	$17/2^{+} \rightarrow 15/2^{+}$	5630.9(3)	4018.7(2)	0.57(3)	-	-	M1
1618.6(1)	$13/2^{-} \rightarrow 9/2^{-}$	3426.0(2)	1807.4(1)	1.14(3)	1.85(9) <sup>&amp;</sup>	0.03(1)	E2
1683.9(1)	$25/2^{+} \rightarrow 21/2^{+}$	8950.8(2)	7266.9(2)	0.66(4)	1.72(10) <sup>&amp;</sup>	0.08(3)	E2
1697.5(1)	$17/2^{(+)} \rightarrow 13/2^{+}$	5729.6(2)	4032.1(2)	0.45(2)	0.95(7) <sup>§</sup>	-	(E2)
1712.2(3)	$15/2^{+} \rightarrow 13/2^{+}$	5147.3(3)	3434.9(2)	0.55(3)	-	-	M1
1720.8(1)	$17/2^{+} \rightarrow 13/2^{+}$	5155.7(2)	3434.9(2)	12.6(2)	1.03(3) <sup>§</sup>	0.04(1)	E2
1740.2(1)	$9/2^{-} \rightarrow 5/2^{-}$	1807.4(1)	67.2(1)	15.4(2)	1.62(8) <sup>&amp;</sup>	0.04(1)	E2
1753.7(2)	$21/2^{+} \rightarrow 17/2^{+}$	7678.9(2)	5925.2(2)	$< 0.2^*$	-	-	E2
1788.0(3)	$13/2^{-} \rightarrow 9/2^{-}$	4197.1(2)	2409.4(1)	0.84(4)	-	-	E2
1822.0(3)	$(31/2^{+}) \rightarrow 27/2^{+}$	10928.8(5)	9106.8(4)	1.37(5)	-	-	(E2)
1835.0(5)	$23/2^{+} \rightarrow 19/2^{+}$	8027.7(2)	6192.9(2)	$< 0.2^*$	-	-	E2
1848.6(2)	$15/2^{+} \rightarrow 11/2^{+}$	5147.3(3)	3298.4(5)	1.43(5)	1.50(8) <sup>&amp;</sup>	-	E2
1875.8(1)	$17/2^{+} \rightarrow 13/2^{+}$	5310.7(2)	3434.9(2)	1.12(5)	1.13(7) <sup>§</sup>	-	E2
1903.8(1)	$13/2^{+} \rightarrow 11/2^{-}$	4032.1(2)	2128.3(1)	2.25(5)	0.75(8) <sup>§</sup>	0.06(2)	E1
1919.8(1)	$9/2^{-} \rightarrow 5/2^{-}$	1987.0(1)	67.2(1)	15.2(2)	1.07(3) <sup>§</sup>	0.07(2)	E2
1945.4(7)	$(35/2^{+}) \rightarrow (31/2^{+})$	12874.2(9)	10928.8(5)	0.79(2)	1.71(9) <sup>&amp;</sup>	-	(E2)
1962.8(5)	$23/2^{+} \rightarrow 19/2^{+}$	8027.7(2)	6065.1(2)	$< 0.2^*$	-	-	E2
2042.4(5)	$(29/2^{+}) \rightarrow 25/2^{+}$	10993.2(6)	8950.8(2)	$< 0.2^*$	-	-	(E2)
2044.9(3)	$13/2^{+} \rightarrow 9/2^{-}$	4032.1(2)	1987.0(1)	0.86(15)	0.97(7) <sup>§</sup>	-	M2
2048.0(4)	$21/2^{+} \rightarrow 17/2^{+}$	7678.9(2)	5630.9(3)	$< 0.2^*$	-	-	E2
2068.8(2)	$13/2^{-} \rightarrow 11/2^{-}$	4197.1(2)	2128.3(1)	2.62(22)	0.46(3) <sup>§</sup>	-	M1+E2
2078.0(2)	$13/2^{+} \rightarrow 11/2^{-}$	4206.3(2)	2128.3(1)	5.3(7)	0.69(5) <sup>§</sup>	-	E1
2078.8(2)	$19/2^{+} \rightarrow 15/2^{+}$	6555.7(3)	4476.9(2)	-#	-	-	E2
2082.2(2)	$21/2^{+} \rightarrow 17/2^{+}$	7237.9(3)	5155.7(2)	-#	0.86(5) <sup>§</sup>	0.14(5)	E2
2085.3(2)	$13/2^{+} \rightarrow 9/2^{+}$	4206.3(2)	2121.0(1)	1.5(6)	1.47(8) <sup>&amp;</sup>	-	E2
2111.2(1)	$21/2^{+} \rightarrow 17/2^{+}$	7266.9(2)	5155.7(2)	1.4(6)	0.86(5) <sup>§</sup>	0.16(9)	E2
2196.0(2)	$17/2^{+} \rightarrow 13/2^{+}$	5630.9(3)	3434.9(2)	0.66(4)	0.88(5) <sup>§</sup>	-	E2
2216.6(2)	$25/2^{+} \rightarrow 21/2^{+}$	8950.8(2)	6734.3(2)	1.45(11)	1.25(9) <sup>§</sup>	-	E2
2224.8(1)	$13/2^{+} \rightarrow 9/2^{-}$	4032.1(2)	1807.4(1)	0.85(12)	-	-	M2
2342.0(1)	$9/2^{-} \rightarrow 5/2^{-}$	2409.4(1)	67.2(1)	2.19(4)	-	-	E2

